



Calculation of predictions for non-identical particle correlations in heavy ions collisions at LHC energies from hydrodynamics-inspired models

MASTER OF SCIENCE THESIS

Author:
Mateusz Wojciech Gałażyn

Supervisor:
Prof. Adam Kisiel

Warsaw, 4th December 2014



Wyznaczenie przewidywań teoretycznych dla korelacji cząstek nieidentycznych w zderzeniach ciężkich jonów przy energiach LHC w modelach opartych na hydrodynamice

PRACA MAGISTERSKA

Autor:
Mateusz Wojciech Gałażyn

Promotor:
dr hab. inż. Adam Kisiel, prof. PW

Warszawa, 4 grudnia 2014

Abstract

This thesis presents results of two-particle momentum correlations analysis for different kinds of particles produced in heavy ion collisions. The studies were carried for the data from lead-lead collisions at the centre of mass energy $\sqrt{s_{NN}} = 2.76$ TeV simulated in the THERMINATOR model using the (3+1)-dimensional hydrodynamic model with viscosity. Analysis was performed for the three particle types: pions, kaons and protons for the collisions in eight different centrality ranges.

The THERMINATOR model allows to perform statistical hadronization of stable particles and unstable resonances from a given hypersurface which is followed by the resonance propagation and decay phase. The four-dimensional hypersurface is coming from the calculations performed on a basis of relativistic hydrodynamic framework with the viscosity corrections.

One can investigate space-time characteristics of the particle-emitting source through two-particle interferometry using experimental observables. The experimental-like analysis of the data coming from a model calculations yields a possibility to test the hydrodynamic description of a quark-gluon plasma. This thesis concentrates on the verification of the prediction of appearance of femtoscopic radii scaling with the transverse mass.

The three dimensional correlation functions were calculated using spherical harmonics decomposition. One can use this approach to perform calculations with lower statistics and moreover the visualization of results is much easier. The calculated correlation functions show expected increase of a correlation for pions and kaons at the low relative momenta of a pair. For the protons at the same momentum region, the decrease occurs. Furthermore, the transverse pair momentum and centrality dependence on a correlation function is observed. In order to perform the quantitative analysis of this influence, the fitting of theoretical formula for correlation function was performed. The femtoscopic radii calculated in the LCMS and PRF are falling with the transverse mass m_T . To test the scaling predicted from the hydrodynamics, the power law was fitted $\alpha m_T^{-\beta}$. The radii calculated for pions, kaons and protons in the LCMS are following the common scaling. In the case of the PRF such scaling is not observed. To recover the scaling in the PRF, the approximate factor is proposed: $\sqrt{(\sqrt{\gamma_T} + 2)/3}$. The radii in the PRF divided by the proposed scaling factor are falling on the common curve, proving that the scaling can be recovered using the proposed factor. The experimental analysis is usually performed in the PRF (requires less statistics), hence the method of scaling recovery enables easier testing of the hydrodynamic predictions, which are not visible in the PRF.

Streszczenie

W tej pracy zaprezentowane są wyniki analizy dwucząstkowych korelacji pędowych dla trzech różnych typów cząstek produkowanych w zderzeniach ciężkich jonów. Obliczenia zostały wykonane dla danych ze zderzeń ołów-ołów przy energii w centrum masy $\sqrt{s_{NN}} = 2.76$ TeV wygenerowanych za pomocą modelu THERMINATOR przy użyciu (3+1)-wymiarowego modelu hydrodynamicznego uwzględniającego lepkość ośrodka. Analiza została wykonana dla trzech rodzajów cząstek: pionów, kaonów i protonów dla dziewięciu różnych przedziałów centralności.

Model THERMINATOR pozwala na wykonanie statystycznej hadronizacji stabilnych cząstek jak i również niestabilnych rezonansów z danej hiperpowierzchni wymrażania, a następnie uwzględnienie propagacji i rozpadów tych rezonansów. Czterowymiarowa hiperpowierzchnia pochodzi z obliczeń przeprowadzonych na podstawie hydrodynamiki relatywistycznej z uwzględnieniem poprawek pochodzących od lepkości.

Interferometria dwucząstkowa pozwala na zbadanie charakterystyk czasowo-przestrzennych źródła cząstek. Poprzez analizę danych pochodzących z obliczeń modelowych można dokonać sprawdzenia zakresu stosownalności hydrodynamiki do opisu właściwości plazmy kwarkowo-gluonowej. Ta praca koncentruje się na weryfikacji skalowania promieni femtoskopowych z masą poprzeczną przewidywanego przez hydrodynamikę.

Wyliczone trójwymiarowe funkcje koreacyjne zostały rozłożone w szereg harmonik sferycznych. To podejście wymaga mniejszej statystyki i pozwala na łatwiejszą wizualizację wyników. Wyliczone funkcje wykazują oczekiwany wzrost korelacji dla niskich różnic pędów dla par pionów i kaonów. Z kolei dla par protonów w tym samym zakresie pędów można zauważać wyraźny spadek korelacji. Przy czym, we wszystkich przypadkach zderzeń jest widoczny wpływ pędu poprzecznego pary oraz centralności na funkcję koreacyjną. W celu wykonania analizy ilościowej tego wpływu, zostało wykonane dopasowanie formuły analitycznej do obliczonych funkcji koreacyjnych. Otrzymane w ten sposób promienie femtoskopowe w LCMS i PRF wykazują spadek wraz z wzrostem masy poprzecznej m_T . W celu sprawdzenie skalowania przewidywanego przez hydrodynamikę została dopasowana zależność potęgowa: $\alpha m_T^{-\beta}$. Promienie obliczone dla pionów, kaonów i protonów zachowują wzajemne skalowanie w LCMS. W przypadku PRF skalowanie nie jest widoczne, więc aby je odzyskać został zaproponowany przybliżony współczynnik skalowania w postaci: $\sqrt{(\sqrt{\gamma_T} + 2)/3}$. Promienie w PRF po podzieleniu przez tą wartość, dają się opisać oczekowaną zależnością potęgową.

⁷⁷ Analiza eksperimentalna jest zazwyczaj wykonywana w PRF, bowiem wy-
⁷⁸ maga w tym układzie odniesienia mniejszej statystyki. Zatem metoda odzyska-
⁷⁹ nia skalowania pozwala na łatwiejszą, w porównaniu z LCMS, weryfikację prze-
⁸⁰ widywania hydrodynamiki, które nie są widoczne w PRF.

⁸¹ Contents

⁸²	Introduction	1
⁸³	1 Theory of heavy ion collisions	3
⁸⁴	1.1 The Standard Model	3
⁸⁵	1.2 Quantum Chromodynamics	4
⁸⁶	1.2.1 Quarks and gluons	4
⁸⁷	1.2.2 Quantum Chromodynamics potential	5
⁸⁸	1.2.3 The quark-gluon plasma	7
⁸⁹	1.3 Relativistic heavy ion collisions	9
⁹⁰	1.3.1 Stages of heavy ion collision	9
⁹¹	1.3.2 QGP signatures	11
⁹²	2 Therminator model	19
⁹³	2.1 (3+1)-dimensional viscous hydrodynamics	19
⁹⁴	2.2 Statistical hadronization	20
⁹⁵	2.2.1 Cooper-Frye formalism	21
⁹⁶	2.3 Events generation procedure	22
⁹⁷	3 Particle interferometry	25
⁹⁸	3.1 HBT interferometry	25
⁹⁹	3.2 Theoretical approach	25
¹⁰⁰	3.2.1 Conventions used	26
¹⁰¹	3.2.2 Two particle wave function	27
¹⁰²	3.2.3 Source emission function	28
¹⁰³	3.2.4 Analytical form of a correlation function	30
¹⁰⁴	3.2.5 Spherical harmonics decomposition of a correlation function	31
¹⁰⁵	3.3 Experimental approach	32
¹⁰⁶	3.4 Scaling of femtoscopic radii	33
¹⁰⁷	3.4.1 Scaling in LCMS	34
¹⁰⁸	3.4.2 Scaling in PRF	35
¹⁰⁹	4 Results	36
¹¹⁰	4.1 Identical particles correlations	36
¹¹¹	4.1.1 Spherical harmonics components	36

112	4.1.2	Centrality dependence of a correlation function	40
113	4.1.3	k_T dependence of a correlation function	41
114	4.2	Results of the fitting procedure	42
115	4.2.1	The three-dimensional femtoscopic radii scaling	43
116	4.2.2	Scaling of one-dimensional radii	46
117	4.3	Discussion of the results	47
118	Conclusions		48
119	A	Scripts for correlation function calculations	50
120	A.1	Events generation	50
121	A.2	Calculations of experimental-like correlation functions	51
122	B	Fitting utilities	52
123	B.1	Minuit package	52
124	B.2	Fitting software	52
125	B.2.1	Input parameters	52
126	B.2.2	Output format	54
127	B.2.3	Compilation	54
128	B.2.4	Usage	54
129	C	Plotting scripts	55
130	C.1	Correlation functions plots	55
131	C.2	Plots with femtoscopic radii	55

¹³² Introduction

Many people were trying to discover what was in the beginning of the Universe which we observe today. Through the years, more or less successful theories were appearing and trying to describe its origin and behaviour. Among them is one model, which provides a comprehensive explanation for a broad range of phenomena, including the cosmic microwave background, abundance of the light elements and Hubble's law. This model is called The Big Bang theory and has been born in 1927 on the basis of the principles proposed by the Belgian priest and scientist Georges Lemaître. Using this model and known laws of physics one can calculate the characteristics of the Universe in detail back in time to the extreme densities and temperatures. However, at some point these calculations fail. The extrapolation of the expansion of the Universe backwards in time using general relativity yields an infinite density and temperature at a finite time in the past. This appearance of singularity is a signal of the breakdown of general relativity. The range of this extrapolation towards singularity is debated - certainly we can go no closer than the end of *Planck epoch* i.e. 10^{-43} s. At this very first era the temperature of the Universe was so high, that the four fundamental forces: electromagnetism, gravitation, weak nuclear interaction and strong nuclear interaction were one fundamental force. Between 10^{-43} s and 10^{-36} s of a lifetime of the Universe, there is a *grand unification epoch*, at which forces are starting to separate from each other. The *electroweak epoch* lasted from 10^{-36} s to 10^{-12} s, when the strong force separated from the electroweak force. After this epoch, there was the *quark epoch* in which the Universe was a dense "soup" of quarks. During this stage the fundamental forces of gravitation, electromagnetism, strong and weak interactions had taken their present forms. The temperature at this moment was still too high to allow quarks to bind together and form hadrons. At the end of quark era, there was a big freeze-out - when the average energy of particle interactions had fallen below the binding energy of hadrons. This era, in which quarks became confined into hadrons, is known as the *hadron epoch*. At this moment the matter had started forming nuclei and atoms, which we observe today.

Here arises the question: how can we study the very beginning of the Universe? To do this, one should recreate in a laboratory appropriate conditions i.e. such large density and high temperature. Today, this is achievable through sophisticated machines like particle accelerators. Sufficiently high energies are available at the Large Hadron Collider at CERN, Geneva and Relativistic Heavy Ion

167 Collider at Brookhaven National Laboratory in Upton, New York. In the particle
168 accelerators the heavy ions after being accelerated to near the speed of light are
169 collided in order to generate extremely dense and hot phase of matter and re-
170 create the quark-gluon plasma. The plasma is believed to behave like an almost
171 ideal fluid, which can be described by the laws of relativistic hydrodynamics.

172 This thesis is providing predictions for collective behaviour of the quark-
173 gluon plasma coming from the hydrodynamic equations. Experimental-like
174 analysis was performed for the high energy Pb-Pb collisions generated with
175 THERMINATOR model.

176 The 1st chapter is an introduction to the theory of heavy ion collisions. It
177 contains the brief description of the Standard Model and Quantum Chromody-
178 namics. Moreover the quark-gluon plasma and its signatures are also here char-
179 acterized.

180 In the 2nd chapter, the relativistic hydrodynamic framework and the
181 THERMINATOR model used to perform the simulations of collisions are
182 described.

183 The 3rd chapter covers the particle interferometry method used in this work.
184 Here are also presented predictions coming from the hydrodynamics, visible in
185 the experimental results. An algorithm of building experimental correlation func-
186 tions is described as well.

187 In the 4th chapter, an interpretation of the results for two-particle femtoscopy
188 for different pairs of particles is presented. Moreover, the quantitative analysis of
189 calculated femtoscopic radii as well as the appearance of transverse mass scaling
190 is discussed.

191 In the Appendices, the detailed description of the tools developed by the au-
192 thor and used in this work is given. Utilities for managing the event generation
193 process and plotting of correlation functions are presented. Furthermore, the fit-
194 ting software, its design and usage is described.

¹⁹⁵ **Chapter 1**

¹⁹⁶ **Theory of heavy ion collisions**

¹⁹⁷ **1.1 The Standard Model**

¹⁹⁸ In the 1970s, a new theory of fundamental particles and their interaction
¹⁹⁹ emerged. It was a new concept, which combines the electromagnetic, weak and
²⁰⁰ strong nuclear interactions between known particles. This theory is called *The*
²⁰¹ *Standard Model*. There are seventeen named particles in the standard model, or-
²⁰² ganized into the chart shown below (Fig. 1.1). Fundamental particles are divided
into two families: *fermions* and *bosons*.

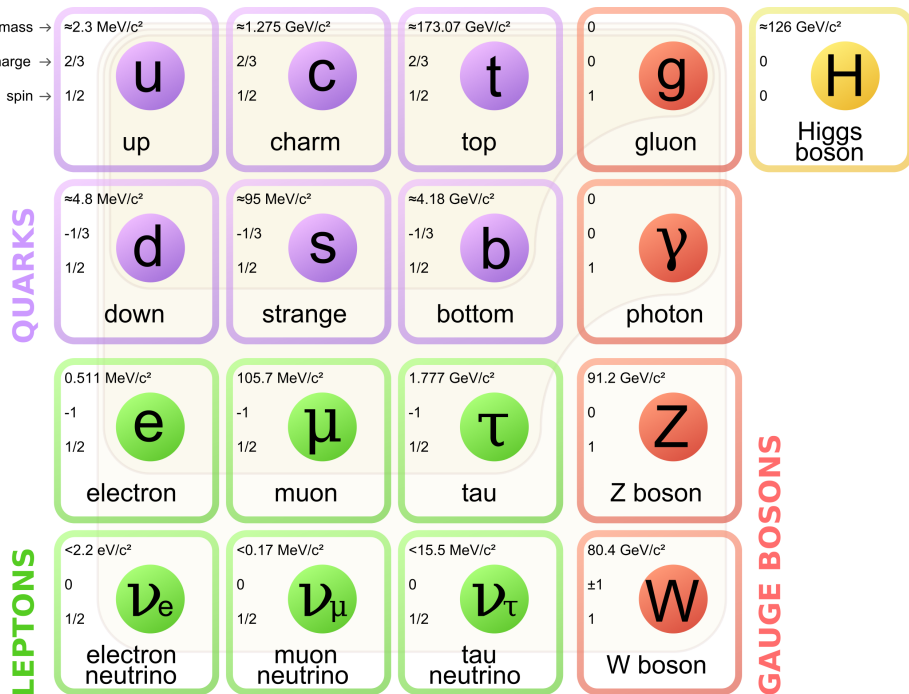


Figure 1.1: The Standard Model of elementary particles [1].

203 Fermions are the building blocks of matter. They are divided into two groups.
 204 Six of them, which must bind together are called *quarks*. Quarks are known to
 205 bind into doublets (*mesons*), triplets (*baryons*) and recently confirmed four-quark
 206 states¹. Two of baryons, with the longest lifetimes, are forming a nucleus: a pro-
 207 ton and a neutron. A proton is build from two up quarks and one down, and
 208 neutron consists of two down quarks and one up. The first one is found to be a
 209 stable particle (at least it has a lifetime larger than 10^{35} years) while a free neutron
 210 has a mean lifetime about 8.8×10^2 s. Fermions that can exist independently are
 211 called *leptons*. Neutrinos are a subgroup of leptons, which are only influenced
 212 by weak interaction. In principle, fermions can be divided into three genera-
 213 tions (three columns in the Figure 1.1). Generation I particles can combine into
 214 hadrons with the longest life spans. Generation II and III consists of unstable
 215 particles which also form unstable hadrons.

216 In turn, bosons are force carriers. There are four fundamental forces: weak -
 217 responsible for radioactive decay, strong - coupling quarks into hadrons, electro-
 218 magnetic - between charged particles and gravity - the weakest, which causes the
 219 attraction between particles with mass. The Standard Model describes the first
 220 three ones. The weak force is mediated by W^\pm and Z^0 bosons, electromagnetic
 221 force is carried by photons γ and the carriers of a strong interaction are gluons
 222 g . Finally, the fifth boson is a Higgs boson which is responsible for giving other
 223 particles mass.

224 1.2 Quantum Chromodynamics

225 1.2.1 Quarks and gluons

226 Quarks interact with each other through the strong interaction. The medi-
 227 ator of this force is a *gluon* - a massless and electrical chargeless particle. In the
 228 quantum chromodynamics (QCD) - theory describing strong interaction - there
 229 are six types of "charges" (like electrical charges in the electrodynamics) called
 230 *colours*. The colours were introduced because some of the observed particles,
 231 like Δ^- , Δ^{++} and Ω^- appeared to consist of three quarks with the same flavour
 232 (ddd , uuu and sss respectively), which was in conflict with the Pauli principle.
 233 One quark can carry one of the three colours (usually called *red*, *green* and *blue*)
 234 while antiquark one of the three anti-colours respectively. Only colour-neutral
 235 (or white) particles could exist. Mesons are assumed to be a colour-anticolour
 236 pair, while baryons are *red-green-blue* triplets. Gluons also are colour-charged
 237 and there are 8 types of gluons. Therefore they can interact with themselves [3].

¹The LHCb experiment at CERN in Geneva confirmed recently the existence of $Z(4430)$ - a particle consisting of four quarks [2].

238 **1.2.2 Quantum Chromodynamics potential**

239 As a result of the fact that gluons are massless, one can expect, that the static
 240 potential in QCD will have the form like similar one in electrodynamics e.g.
 241 $\sim 1/r$ (by analogy to photons). In reality the QCD potential is assumed to have
 242 the form of [3]:

$$V_s = -\frac{4}{3} \frac{\alpha_s}{r} + kr, \quad (1.1)$$

243 where the α_s is a coupling constant of the strong force and the kr part is related
 244 with *confinement*. In comparison to the electromagnetic force, a value of the strong
 245 coupling constant is $\alpha_s \approx 1$ and the electromagnetic one is $\alpha = 1/137$.

246 The fact that quarks does not exist separately and are always bound, is called
 247 confinement. As two quarks are pulled apart, the linear part kr in the Eq. 1.1
 248 becomes dominant and the potential becomes proportional to the distance. This
 249 situation resembles stretching of a string. At some point, when the string is so
 250 large it is energetically favourable to create a quark-antiquark pair. After form-
 251 ation of such pair (or pairs), the string breaks and the confinement is preserved
 (Fig. 1.2).

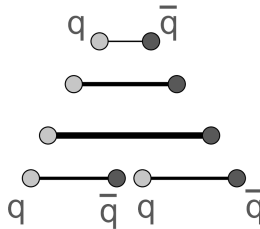


Figure 1.2: A string breaking and a creation of a new quark-antiquark pair [4].

252
 253 On the other hand, for small r , an interaction between the quarks and gluons
 254 is dominated by the Coulomb-like term $-\frac{4}{3} \frac{\alpha_s}{r}$. The coupling constant α_s depends
 255 on the four-momentum Q^2 transferred in the interaction. This dependence is
 256 presented in Fig. 1.3. The value α_s decreases with increasing momentum trans-
 257 fer and the interaction becomes weak for large Q^2 , i.e. $\alpha_s(Q) \rightarrow 0$. Because of
 258 the weakening of coupling constant, quarks at large energies (or small distances)
 259 are starting to behave like free particles. This phenomenon is known as *asym-*
 260 *ptotic freedom*. The QCD potential exhibits also a temperature dependence - the
 261 force strength "melts" with the temperature increase. Therefore the asymptotic
 262 freedom is expected to appear in either the case of high baryon densities (small
 263 distances between quarks) or very high temperatures. This temperature depend-
 264 ence is illustrated in Fig. 1.4.

265 If the coupling constant α_s is small, one can use perturbative methods to cal-
 266 culate physical observables. Perturbative QCD (pQCD) successfully describes
 267 hard processes (with large Q^2) such as jet production in high energy proton-
 268 antiproton collisions. The applicability of pQCD is defined by the *scale para-*
 269 *meter* $\Lambda_{QCD} \approx 200$ MeV. If $Q \gg \Lambda_{QCD}$ then the process is in the perturbative



Figure 1.3: The coupling parameter α_s dependence on four-momentum transfer Q^2 [5].

domain and can be described by pQCD. A description of soft processes (when $Q < 1$ GeV) is a problem in QCD - perturbative theory breaks down at this scale. Therefore, to describe reactions with low Q^2 , one has to use alternative methods like Lattice QCD. Lattice QCD (LQCD) is non-perturbative implementation of a field theory in which QCD quantities are calculated on a discrete space-time grid. LQCD allows to obtain properties of matter in equilibrium, but there are some limitations. First of all, Lattice QCD requires fine lattice spacing to obtain precise results. Therefore large computational resources are necessary. However, nowadays with the constant growth of computing power this problem will become less important. The second problem is that lattice simulations are possible only for baryon density $\mu_B = 0$. At $\mu_B \neq 0$, Lattice QCD breaks down because of the sign problem. In QCD the thermodynamic observables are related to the grand canonical partition function, which has a baryonic chemical potential μ_B as a parameter. Therefore, the baryonic density can be controlled by tuning the baryonic chemical potential. For fermions μ_B can be both positive and negative. For particles with μ_B , their antiparticles have chemical potentials with opposite sign $-\mu_B$. Since at the early universe the number of baryons and antibaryons were almost equal we can use $\mu_B = 0$ to a very good approximation [6].

1.2.3 The quark-gluon plasma

The new state of matter in which quarks are no longer confined is known as a *quark-gluon plasma* (QGP). The predictions coming from the discrete space-time

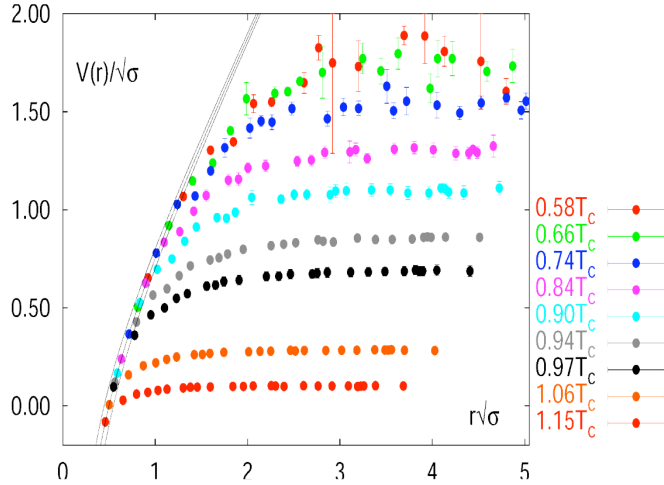


Figure 1.4: The QCD potential for a quark-antiquark pair as a function of distance for different temperatures. A value of a potential decreases with the temperature [4].

291 Lattice QCD calculations reveal a phase transition from the hadronic matter to
 292 the quark-gluon plasma at the high temperatures and baryon densities. The res-
 293 ults obtained from such calculations are shown on Fig. 1.5. The energy density
 294 ϵ which is divided by T^4 is a measure of the number of degrees of freedom in
 295 the system. One can observe significant rise of this value, when the temperat-
 296 ure increases past the critical value T_C . Such increase is signaling a phase transi-
 297 - the formation of QGP [8]. The values of the energy densities plotted in Fig. 1.5
 298 do not reach the Stefan-Boltzmann limit ϵ_{SB} (marked with arrows), which corres-

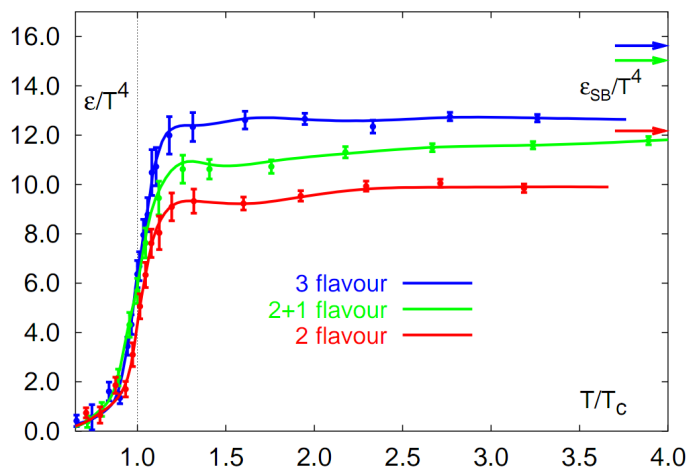


Figure 1.5: A number of degrees of freedom as a function of a temperature [7].

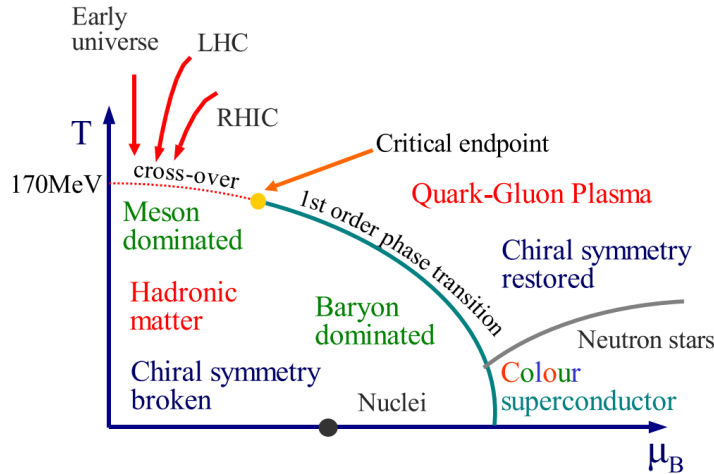


Figure 1.6: Phase diagram coming from the Lattice QCD calculations [8].

ponds to an ideal gas. This can indicate some residual interactions in the system.
According to the results from the RHIC², the new phase of matter behaves more
like an ideal fluid, than like a gas [9].

One of the key questions, to which current heavy ion physics tries to find an answer is the value of a critical temperature T_C as a function of a baryon chemical potential μ_B (baryon density), where the phase transition occurs. The results coming from the Lattice QCD are presented in Fig. 1.6. The phase of matter in which quarks and gluons are deconfined is expected to exist at large temperatures. In the region of small temperatures and high baryon densities, a different state is supposed to appear - a *colour superconductor*. The phase transition between hadronic matter and the QGP is thought to be of 1st order at $\mu_B \gg 0$. However as $\mu_B \rightarrow 0$ quarks' masses become significant and a sharp transition transforms into a rapid but smooth cross-over. It is believed that in Pb-Pb collisions observed at the LHC³, the created matter has high enough temperature to be in the quark-gluon plasma phase, then cools down and converts into hadrons, undergoing a smooth transition [8].

1.3 Relativistic heavy ion collisions

1.3.1 Stages of heavy ion collision

To create the quark-gluon plasma one has to achieve high enough temperatures and baryon densities. Such conditions can be recreated in the heavy ion collisions at the high energies. The left side of the Figure 1.7 shows simplified

²Relativistic Heavy Ion Collider at Brookhaven National Laboratory in Upton, New York

³Large Hadron Collider at CERN, Geneva

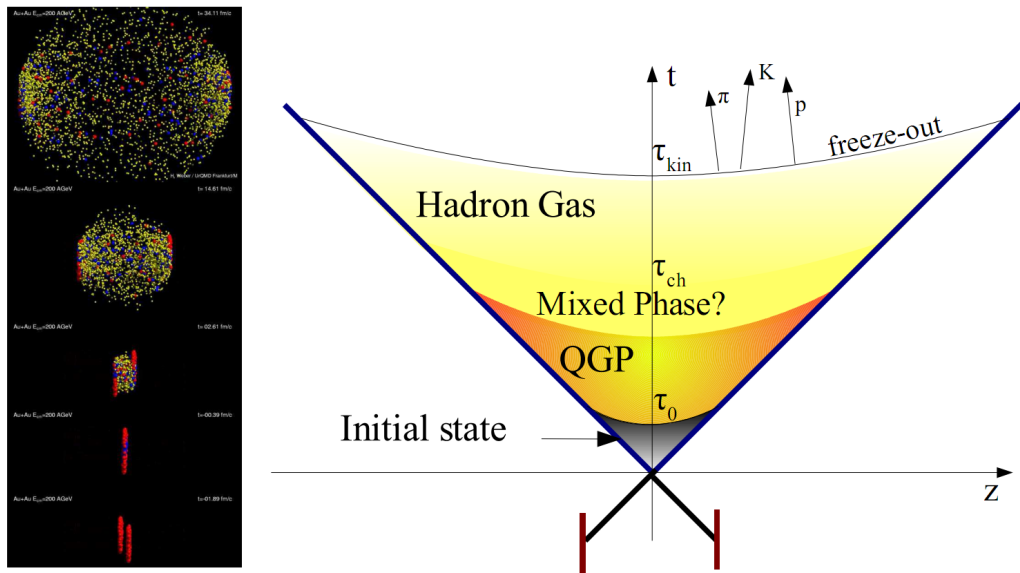


Figure 1.7: Left: stages of a heavy ion collision simulated in the UrQMD model. Right: schematic view of a heavy ion collision evolution [8].

320 picture of a central collision of two highly relativistic nuclei in the centre-of-
 321 mass reference frame. The colliding nuclei are presented as thin disks because
 322 of the Lorentz contraction. In the central region, where the energy density is the
 323 highest, a new state of matter - the quark-gluon plasma - is supposedly created.
 324 Afterwards, the plasma expands and cools down, quarks combine into hadrons
 325 and their mutual interactions cease when the system reaches the *freeze-out* tem-
 326 perature. Subsequently, produced free hadrons move towards the detectors.

327 On the right side of the Figure 1.7 a space-time evolution of a collision process
 328 is presented, plotted in the light-cone variables (z, t). The two highly relativistic
 329 nuclei are traveling basically along the light cone until they collide at the centre
 330 of the diagram. Nuclear fragments emerge from the collision again along the
 331 (forward) light cone, while the matter between fragmentation zones populates
 332 the central region. This hot and dense matter is believed to be in the state of the
 333 quark-gluon plasma. Several frameworks exist to describe this transition to the
 334 QGP phase, for example: QCD string breaking, QCD parton cascades or colour
 335 glass condensate evolving into glasma and later into quark-gluon plasma [10].

336 **String breaking** – In the string picture, the nuclei pass through each other form-
 337 ing colour strings. This is analogous to the situation depicted in the Fig 1.2 - the
 338 colour string is created between quarks inside particular nucleons in nuclei. In
 339 the next step strings decay / fragment forming quarks and gluons or directly
 340 hadrons. This approach becomes invalid at very high energies, when the strings
 341 overlap and cannot be treated as independent objects.

342 Parton cascade – The parton⁴ cascade model is based on the pQCD. The collid-
343 ing nuclei are treated as clouds of quarks which penetrate through each other.
344 The key element of this method is the time evolution of the parton phase-space
345 distributions, which is governed by a relativistic Boltzmann equation with a col-
346 lision term that contains dominant perturbative QCD interactions. The bottleneck
347 of the parton cascade model is the low energies regime, where the Q^2 is too small
348 to be described by the perturbative theory.

349 Colour glass condensate – The colour glass condensate assumes, that the had-
350 ron can be viewed as a tightly packed system of interacting gluons. The sat-
351 uration of gluons increases with energy, hence the total number of gluons may
352 increase without bound. Such a saturated and weakly coupled gluon system is
353 called a colour glass condensate. The fast gluons in the condensate are Lorentz
354 contracted and redistributed on the two very thin sheets representing two col-
355 liding nuclei. The sheets are perpendicular to the beam axis. The fast gluons
356 produce mutually orthogonal colour magnetic and electric fields, that only ex-
357 ist on the sheets. Immediately after the collision, i.e. just after the passage of
358 the two gluonic sheets through each other, the longitudinal electric and magnetic
359 fields are produced forming the *glasma*. The glasma fields decay through the
360 classical rearrangement of the fields into radiation of gluons. Also decays due to
361 the quantum pair creations are possible. In this way, the quark-gluon plasma is
362 produced.

363 Interactions within the created quark-gluon plasma bring the system into
364 the local statistical equilibrium, hence its further evolution can be described by
365 the relativistic hydrodynamics. The hydrodynamic expansion causes the sys-
366 tem to become more and more dilute. The phase transition from the quark-gluon
367 plasma to the hadronic gas occurs. Further expansion causes a transition from the
368 strongly interaction hadronic gas to weakly interacting system of hadrons which
369 move freely to the detectors. Such decoupling of hadrons is called the *freeze-out*.
370 The freeze-out can be divided into two phases: the chemical freeze-out and the
371 thermal one. The *chemical freeze-out* occurs when the inelastic collisions between
372 constituents of the hadron gas stop. As the system evolves from the chemical
373 freeze-out to the thermal freeze-out the dominant processes are elastic collisions
374 (such as, for example $\pi + \pi \rightarrow \rho \rightarrow \pi + \pi$) and strong decays of heavier reso-
375 nances which populate the yield of stable hadrons. The *thermal freeze-out* is the
376 stage of the evolution of matter, when the strongly coupled system transforms
377 to a weakly coupled one (consisting of essentially free particles). In other words
378 this is the moment, where the hadrons practically stop to interact. Obviously, the
379 temperatures corresponding to the two freeze-outs satisfy the condition

$$T_{chem} > T_{therm}, \quad (1.2)$$

380 where T_{chem} (inferred from the ratios of hadron multiplicities) is the temperature
381 of the chemical freeze-out, and T_{therm} (obtained from the investigation of the

⁴A parton is a common name for a quark and a gluon.

382 transverse-momentum spectra) is the temperature of the thermal freeze-out [10].

383 **1.3.2 QGP signatures**

384 The quark-gluon plasma is a very short living and unstable state of matter.
 385 One cannot investigate the properties of a plasma and confirm its existence di-
 386 rectly. Hence, the several experimental effects were proposed as QGP signatures,
 387 some of them have been already observed in heavy ion experiments [8]. As mat-
 388 ter created in the heavy ions collisions is supposed to behave like a fluid, one
 389 should expect appearance of collective behaviour at small transverse momenta
 390 - so called *elliptic flow* and *radial flow*. The next signal is the temperature range
 391 obtained from the measurements of *direct photons*, which gives us information,
 392 that the system created in heavy ion collisions is far above the critical temperat-
 393 ure obtained from the LQCD calculations. The *puzzle in the di-lepton spectrum* can
 394 be explained by the modification of spectral shape of vector mesons (mostly ρ
 395 meson) in the presence of a dense medium. This presence of a medium can also
 396 shed light on the *jet quenching* phenomenon - the suppression occurrence in the
 397 high p_T domain.

398 **Elliptic flow**

399 In a non-central heavy ion collisions, created region of matter has an almond
 400 shape with its shorter axis in the *reaction plane* (Fig. 1.8). The pressure gradient
 401 is much larger in-plane rather than out-of-plane. This causes larger acceleration
 402 and transverse velocities in-plane rather than out-of-plane. Such differences can
 403 be investigated by studying the distribution of particles with respect to the reac-

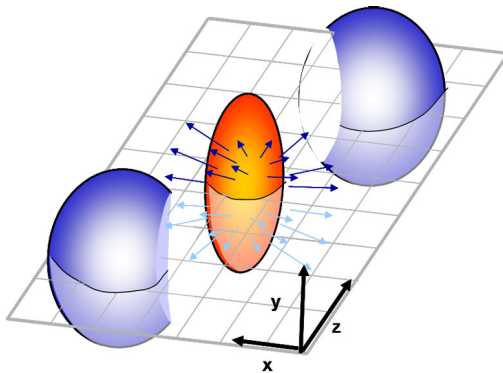


Figure 1.8: Overlapping region which is created in heavy ion collisions has an almond shape. Visible x-z plane is a *reaction plane*. The x-y plane is a *transverse plane*. The z is a direction of the beam [11].

404 tion plane orientation [12]:

$$E \frac{d^3 N}{dp^3} = \frac{1}{2\pi} \frac{d^2 N}{p_T dp_T dy} (1 + 2v_1 \cos(\phi) + 2v_2 \cos(2\phi) + \dots), \quad (1.3)$$

405 where ϕ is the angle between particle transverse momentum p_T (a momentum
 406 projection on a transverse plane) and the reaction plane, N is a number of
 407 particles and E is an energy of a particle. The y variable is *rapidity* defined as:

$$y = \frac{1}{2} \ln \left(\frac{E + p_L}{E - p_L} \right), \quad (1.4)$$

408 where p_L is a longitudinal component of a momentum (parallel to the beam direction). The v_n coefficients indicate the shape of a system. For the most central collisions (b = 0 - see Fig. 1.9) all coefficients vanish $\sum_{n \in N_+} v_n = 0$ (the overlapping region has the spherical shape). The Fourier series elements in the parentheses in Eq. 1.3 represent different kinds of flow. The first value: "1" represents the *radial flow* - an isotropic flow in every direction. Next coefficient v_1 is responsible for *direct flow*. The v_2 coefficient is a measure of elliptic anisotropy (*elliptic flow*). The v_2 has to build up in the early stage of a collision - later the system becomes too dilute: space asymmetry and the pressure gradient vanish. Therefore the observation of elliptic flow means that the created matter was in fact a strongly interacting matter.

409 The v_2 coefficient was measured already at CERN SPS, LHC and RHIC. For
 410 the first time hydrodynamics successfully described the collision dynamics as the
 411 measured v_2 reached hydrodynamic limit (Fig. 1.10). As expected, there is a mass
 412 ordering of v_2 as a function of p_T (lower plot in the Fig. 1.10) with pions having

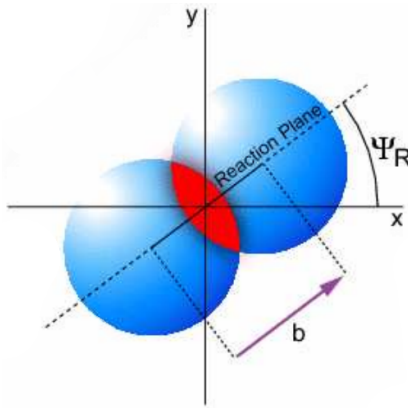


Figure 1.9: Cross-section of a heavy ion collision in a transverse plane. The b parameter is an *impact parameter* - a distance between centers of nuclei during a collision. An impact parameter is related with the centrality of a collision and a volume of the quark-gluon plasma [12].

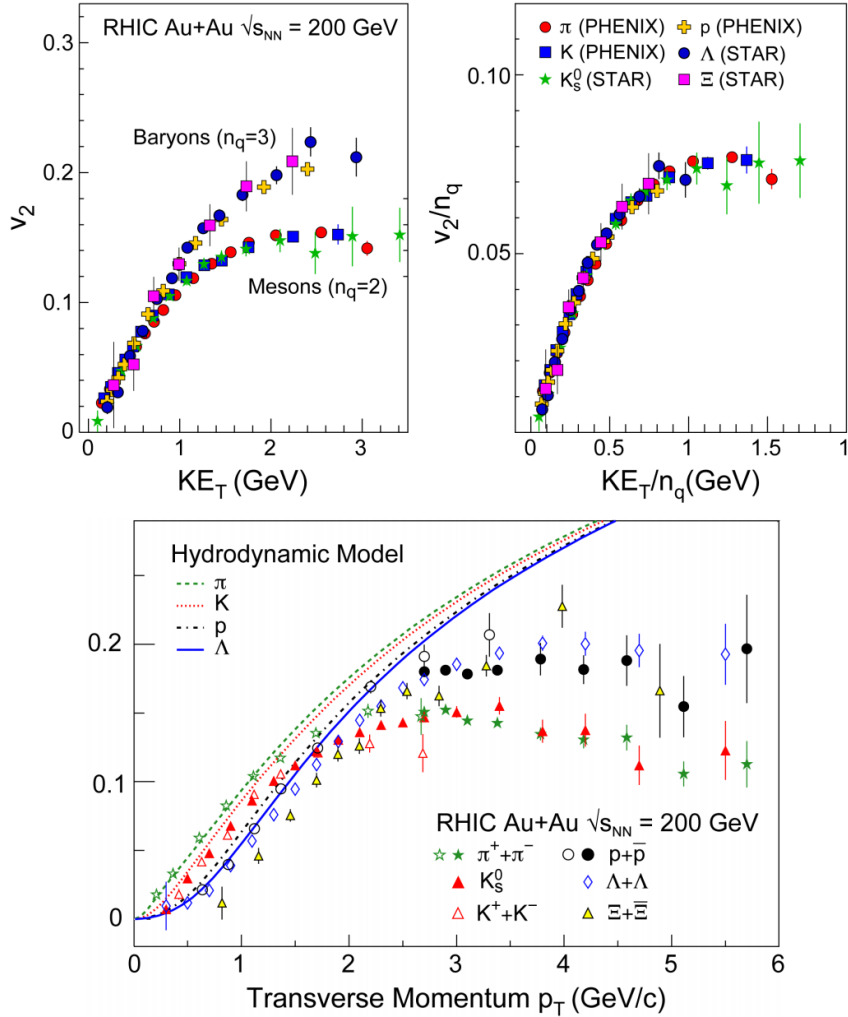


Figure 1.10: *Lower:* The elliptic flow v_2 follows the hydrodynamical predictions for an ideal fluid perfectly. Note that > 99% of all final hadrons have $p_T < 1.5 \text{ GeV}/c$. *Upper left:* The v_2 plotted versus transverse kinetic energy $KE_T = m_T - m_0 = \sqrt{p_T^2 + m_0^2} - m_0$. The v_2 follows different universal curves for mesons and baryons. *Upper right:* When scaled by the number of valence quarks, the v_2 follows the same universal curve for all hadrons and for all values of scaled transverse kinetic energy [13].

423 the largest and protons the smallest anisotropy. In the upper plots in the Fig. 1.10
 424 there is a v_2 as a function of transverse kinetic energy. The left plot shows two
 425 universal trend lines for baryons and mesons. After the scaling of v_2 and the
 426 kinetic energy by the number of valence quarks, all of the hadrons follow the
 427 same universal curve. Those plots show that strong collectivity is observed in

428 heavy ion collisions.

429 **Transverse radial flow**

430 Elliptic flow described previously is caused by the pressure gradients which
 431 must also produce a more simple collective behaviour of matter - a movement
 432 inside-out, called radial flow. Particles are pushed to higher momenta and they
 433 move away from the center of the collision. A source not showing collective
 434 behaviour, like pp collisions, produces particle spectra that can be fitted by a
 435 power-law [8]:

$$\frac{1}{2\pi p_T} \frac{d^2N}{dp_T d\eta} = C \left(1 + \frac{p_T}{p_0} \right)^{-n} . \quad (1.5)$$

436 The η variable is *pseudorapidity* defined as follows:

$$\eta = \frac{1}{2} \ln \left(\frac{p + p_L}{p - p_L} \right) = -\ln \left(\frac{\theta}{2} \right) , \quad (1.6)$$

where θ is an emission angle $\cos \theta = p_L/p$.

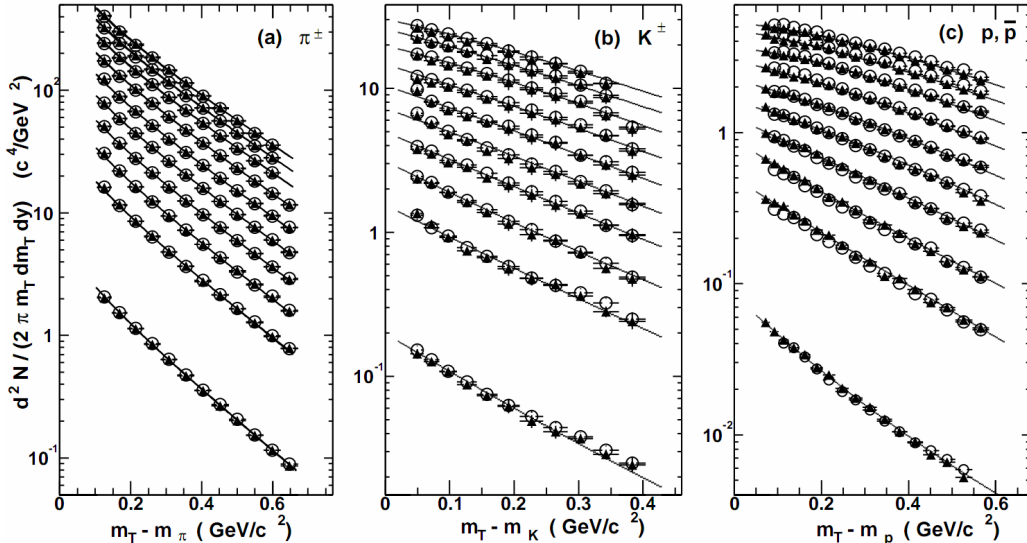


Figure 1.11: Invariant yield of particles versus transverse mass $m_T = \sqrt{p_T^2 + m_0^2}$ for π^\pm , K^\pm , p and \bar{p} at mid-rapidity for p+p collisions (bottom) and Au+Au events from 70-80% (second bottom) to 0-5% (top) centrality [14].

437
 438 The hydrodynamical expansion of a system gives the same flow velocity kick
 439 for different kinds of particles - ones with bigger masses will gain larger p_T boost.
 440 This causes increase of the yield of particles with larger transverse momenta. In
 441 the invariant yield plots one can observe the decrease of the slope parameter,
 442 especially for the heavier hadrons. This is presented in the Fig. 1.11. The most

443 affected spectra are ones of kaons (b) and protons (c). One can notice decrease
 444 of the slope parameter for heavy ion collisions (plots from second bottom to top)
 445 comparing to the proton-proton collisions (bottom ones), where no boost from
 446 radial flow should occur [8].

447 Another signature of a transverse radial flow is a dependence of HBT radii on
 448 a pair transverse momentum. Detailed description of this effect is presented in
 449 the Section 3.4.

450 Direct photons

451 The direct photons are photons, which are not coming from the final state
 452 hadrons decays. Their sources can be various interaction from charged particles
 453 created in the collision, either at the partonic or at the hadronic level. Direct
 454 photons are considered to be an excellent probe of the early stage of the collision.
 455 This is because their mean free path is very large when compared to the size of
 456 created system in the collision. Thus photons created at the early stage leave the
 457 system without suffering any interaction and retain information about this stage,
 458 in particular about its temperature.

459 One can distinguish two kinds of direct photons: *thermal* and *prompt*. Thermal
 460 photons can be emitted from the strong processes in the quark-gluon plasma in-

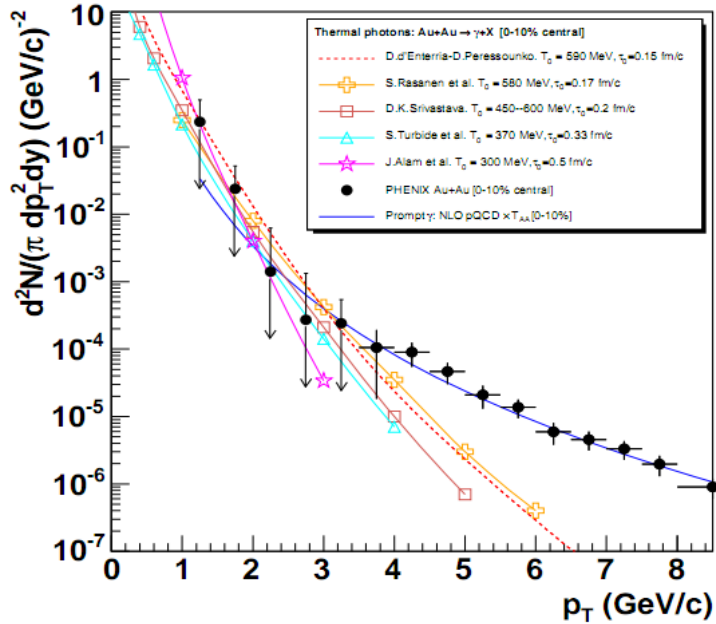


Figure 1.12: Thermal photons spectra for the central Au+Au collisions at $\sqrt{s_{NN}} = 200$ GeV computed within different hydrodynamical models compared with the pQCD calculations (solid line) and experimental data from PHENIX (black dots) [15].

volving quarks and gluons or hot hadronic matter (e.g. processes: $\pi\pi \rightarrow \rho\gamma$, $\pi\rho \rightarrow \pi\gamma$). Thermal photons can be observed in the low p_T region. Prompt photons are believed to come from “hard” collisions of initial state partons belonging to the colliding nuclei. The prompt photons can be described using the pQCD. They will dominate the high p_T region. The analysis of transverse momentum of spectra of direct photons revealed, that the temperature of the source of thermal photons produced in heavy ion collisions at RHIC is in the range 300–600 MeV (Fig. 1.12). Hence the direct photons had to come from a system whose temperature is far above from the critical temperature for QGP creation.

470 Puzzle in di-lepton mass spectrum

The invariant mass spectra (Fig. 1.13) of lepton pairs reveal many peaks corresponding to direct decays of various mesons into a lepton pair. The continuous background in this plot is caused by the decays of hadrons into more than two leptons (including so-called *Dalitz decays* into a lepton pair and a photon). Particular hadron decay channels, which contribute to this spectrum are shown

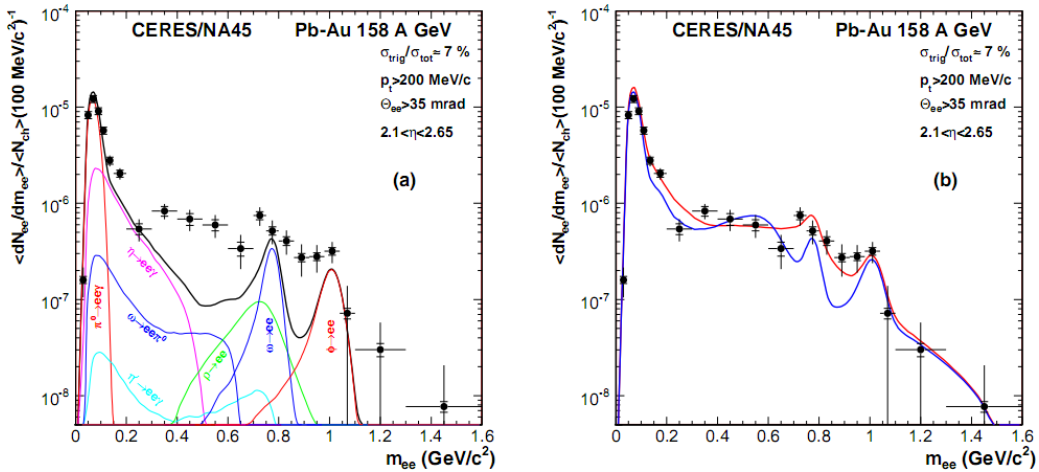


Figure 1.13: Left: Invariant mass spectrum of $e^+ - e^-$ pairs in Pb+Au collisions at 158A GeV compared to the sum coming from the hadron decays predictions. Right: The expectations coming from model calculations assuming a dropping of the ρ mass (blue) or a spread of the ρ width in the medium (red) [16].

in Fig. 1.13 with the coloured lines and their sum with the black one. The sum (called *the hadronic cocktail*) of various components describes experimental spectra coming from the simple collisions (like p+p or p+A) quite well with the statistical and systematical uncertainties [9]. This situation is different considering more complicated systems i.e. A+A. Spectra coming from Pb+Au collisions are presented on the plots in the Fig. 1.13. The “hadronic cocktail” does not describe the data, in the mass range between the π and the ρ mesons a significant excess of electron pairs over the calculated sum is observed. Theoretical explanation of

484 this phenomenon assumes modification of the spectral shape of vector mesons in
 485 a dense medium. Two different interpretations of this increase were proposed:
 486 a decrease of meson mass with the medium density and increase of the meson
 487 width in the dense medium. In principle, one could think of simultaneous oc-
 488 currence of both effects: mass shift and resonance broadening. Experimental res-
 489 ults coming from the CERES disfavour the mass shift hypothesis indicating only
 490 broadening of resonance peaks (Fig. 1.13b) [9].

491 Jet quenching

492 A jet is defined as a group of particles with close vector momenta and high en-
 493 ergies. It has its beginning when the two partons are going in opposite directions
 494 and have energy big enough to produce new quark-antiquark pair and then ra-
 495 diate gluons. This process can be repeated many times and it results in two back-
 496 to-back jets of hadrons. It has been found that jets in the opposite hemisphere
 497 (*away-side jets*) show a very different pattern in d+Au and Au+Au collisions. This
 498 is shown in the azimuthal correlations in the Fig. 1.14. In d+Au collisions, like
 499 in p+p, a pronounced away-side jet appears around $\Delta\phi = \pi$, exactly opposite
 500 to the trigger jet, which is typical for di-jet events. In central Au+Au collisions
 501 the away-side jet is suppressed. When the jet has its beginning near the surface
 502 of the quark-gluon plasma, one of the jets (*near-side jet*) leaves the system almost
 503 without any interactions. This jet is visible on the correlation plot as a high peak
 504 at $\Delta\phi = 0$. However, the jet moving towards the opposite direction has to pen-
 505 etrate a dense medium. The interaction with the plasma causes energy dissipation

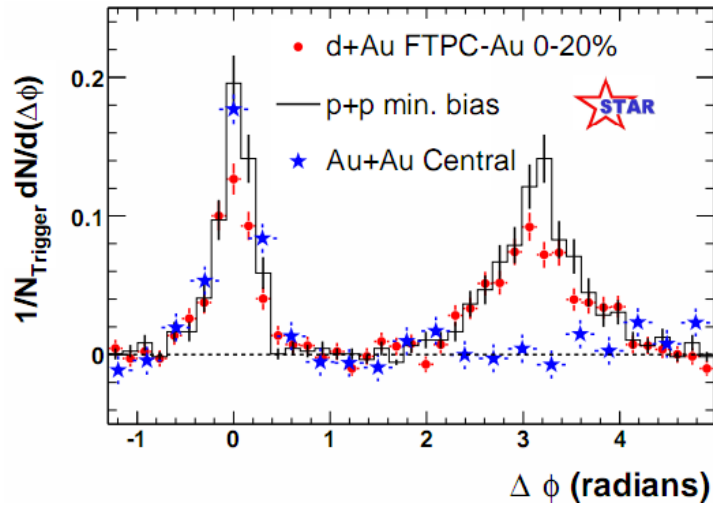


Figure 1.14: Azimuthal angle difference $\Delta\phi$ distributions for different colliding systems at $\sqrt{s_{NN}} = 200$ GeV. Transverse momentum cut: $p_T > 2$ GeV. For the Au+Au collisions the away-side jet is missing [17].

506 of particles and is visible on an azimuthal correlation plot as a disappearance of
507 the away-side jet [9].

508 **Chapter 2**

509 **Therminator model**

510 THERMINATOR [18] is a Monte Carlo event generator designed to investigate
511 the particle production in the relativistic heavy ion collisions. The functionality
512 of the code includes a generation of the stable particles and unstable resonances
513 at the chosen hypersurface model. It performs the statistical hadronization which
514 is followed by space-time evolution of particles and the decay of resonances. The
515 key element of this method is an inclusion of a complete list of hadronic reso-
516 nances, which contribute very significantly to the observables. The second version
517 of THERMINATOR [19] comes with a possibility to incorporate any shape of freeze-
518 out hypersurface and the expansion velocity field, especially those generated ex-
519 ternally with various hydrodynamic codes. The event generator is written in C++
520 programming language and it employs ROOT [20] analysis framework.

521 **2.1 (3+1)-dimensional viscous hydrodynamics**

522 Most of the relativistic viscous hydrodynamic calculations are done in
523 (2+1)-dimensions. Such simplification assumes boost-invariance of a matter
524 created in a collision. Experimental data reveals that no boost-invariant region is
525 formed in the collisions [21]. Hence, for the better description of created system
526 a (3+1)-dimensional model is required.

527 In the four dimensional relativistic dynamics one can describe a system
528 using a space-time four-vector $x^\nu = (ct, x, y, z)$, a velocity four-vector
529 $u^\nu = \gamma(c, v_x, v_y, v_z)$ and a energy-momentum tensor $T^{\mu\nu}$. The particular
530 components of $T^{\mu\nu}$ have a following meaning:

- 531 • T^{00} - an energy density,
- 532 • $cT^{0\alpha}$ - an energy flux across a surface x^α ,
- 533 • $T^{\alpha 0}$ - an α -momentum flux across a surface x^α multiplied by c ,
- 534 • $T^{\alpha\beta}$ - components of momentum flux density tensor,

535 where $\gamma = (1 - v^2/c^2)^{-1/2}$ is Lorentz factor and $\alpha, \beta \in \{1, 2, 3\}$. Using u^ν one can
 536 express $T^{\mu\nu}$ as follows [22]:

$$T_0^{\mu\nu} = (e + p)u^\mu u^\nu - pg^{\mu\nu} \quad (2.1)$$

537 where e is an energy density, p is a pressure and $g^{\mu\nu}$ is an inverse metric tensor:

$$g^{\mu\nu} = \begin{bmatrix} 1 & 0 & 0 & 0 \\ 0 & -1 & 0 & 0 \\ 0 & 0 & -1 & 0 \\ 0 & 0 & 0 & -1 \end{bmatrix}. \quad (2.2)$$

538 The presented version of energy-momentum tensor (Eq. 2.1) can be used to de-
 539 scribe dynamics of a perfect fluid. To take into account influence of viscosity,
 540 one has to apply the following corrections coming from shear $\pi^{\mu\nu}$ and bulk Π
 541 viscosities [23]:

$$T^{\mu\nu} = T_0^{\mu\nu} + \pi^{\mu\nu} + \Pi(g^{\mu\nu} - u^\mu u^\nu). \quad (2.3)$$

542 The stress tensor $\pi^{\mu\nu}$ and the bulk viscosity Π are solutions of dynamical equa-
 543 tions in the second order viscous hydrodynamic framework [22]. The compari-
 544 son of hydrodynamics calculations with the experimental results reveal, that the
 545 shear viscosity divided by entropy η/s has to be small and close to the AdS/CFT
 546 estimate $\eta/s = 0.08$ [23, 24]. The bulk viscosity over entropy value used in calcu-
 547 lations is $\zeta/s = 0.04$ [23].

548 When using $T^{\mu\nu}$ to describe system evolving close to local thermodynamic
 549 equilibrium, relativistic hydrodynamic equations in a form of:

$$\partial_\mu T^{\mu\nu} = 0 \quad (2.4)$$

550 can be used to describe the dynamics of the local energy density, pressure and
 551 flow velocity.

552 Hydrodynamic calculations are starting from the Glauber¹ model initial con-
 553 ditions. The collective expansion of a fluid ends at the freeze-out hypersurface.
 554 That surface is usually defined as a constant temperature surface, or equivalently
 555 as a cut-off in local energy density. The freeze-out is assumed to occur at the
 556 temperature $T = 140$ MeV.

557 2.2 Statistical hadronization

558 Statistical description of heavy ion collision has been successfully used to
 559 quantitatively describe the *soft* physics, i.e. the regime with the transverse mo-
 560 mentum not exceeding 2 GeV. The basic assumption of the statistical approach of
 561 evolution of the quark-gluon plasma is that at some point of the space-time evol-
 562 ution of the fireball, the thermal equilibrium is reached. When the system is in the

¹The Glauber Model is used to calculate “geometrical” parameters of a collision like an impact parameter, number of participating nucleons or number of binary collisions.

563 thermal equilibrium the local phase-space densities of particles follow the Fermi-
 564 Dirac or Bose-Einstein statistical distributions. At the end of the plasma expan-
 565 sion, the freeze-out occurs. The freeze-out model incorporated in THERMINATOR
 566 assumes, that chemical and thermal freeze-outs occur at the same time.

567 **2.2.1 Cooper-Frye formalism**

568 The result of the hydrodynamic calculations is the freeze-out hyper-
 569 surface Σ^μ . A three-dimensional element of the surface is defined as [19]

$$570 \quad d\Sigma_\mu = \epsilon_{\mu\alpha\beta\gamma} \frac{\partial x^\alpha}{\partial \alpha} \frac{\partial x^\beta}{\partial \beta} \frac{\partial x^\gamma}{\partial \gamma} d\alpha d\beta d\gamma, \quad (2.5)$$

571 where $\epsilon_{\mu\alpha\beta\gamma}$ is the Levi-Civita tensor and the variables $\alpha, \beta, \gamma \in \{1, 2, 3\}$ are used
 572 to parametrize the three-dimensional freeze-out hypersurface in the Minkowski
 573 four-dimensional space. The Levi-Civita tensor is equal to 1 when the indices
 574 form an even permutation (eg. ϵ_{0123}), to -1 when the permutation is odd (e.g.
 575 ϵ_{2134}) and has a value of 0 if any index is repeated. Therefore [19],

$$576 \quad d\Sigma_0 = \begin{vmatrix} \frac{\partial x}{\partial \alpha} & \frac{\partial x}{\partial \beta} & \frac{\partial x}{\partial \gamma} \\ \frac{\partial y}{\partial \alpha} & \frac{\partial y}{\partial \beta} & \frac{\partial y}{\partial \gamma} \\ \frac{\partial z}{\partial \alpha} & \frac{\partial z}{\partial \beta} & \frac{\partial z}{\partial \gamma} \end{vmatrix} d\alpha d\beta d\gamma \quad (2.6)$$

576 and the remaining components are obtained by cyclic permutations of t, x, y
 577 and z .

One can obtain the number of hadrons produced on the hypersurface Σ^μ from
 the Cooper-Frye formalism. The following integral yields the total number of
 created particles [19]:

$$577 \quad N = (2s + 1) \int \frac{d^3 p}{(2\pi)^3 E_p} \int d\Sigma_\mu p^\mu f(p_\mu u^\mu), \quad (2.7)$$

578 where $f(p_\mu u^\mu)$ is the phase-space distribution of particles (for stable ones and res-
 579 onances). One can simply derive from Eq. 2.7, the dependence of the momentum
 580 density [25]:

$$581 \quad E \frac{d^3 N}{dp^3} = \int d\Sigma_\mu f(p_\mu u^\mu) p^\mu. \quad (2.8)$$

581 The momentum distribution f contains non-equilibrium corrections:

$$582 \quad f = f_0 + \delta f_{shear} + \delta f_{bulk}, \quad (2.9)$$

582 where

$$583 \quad f_0(p_\mu u^\mu) = \left\{ \exp \left[\frac{p_\mu u^\mu - (B\mu_B + I_3\mu_{I_3} + S\mu_S + C\mu_C)}{T} \right] \pm 1 \right\}^{-1}. \quad (2.10)$$

583 In case of fermions, in the Eq. 2.10 there is a plus sign and for bosons, minus
 584 sign respectively. The thermodynamic quantities appearing in the $f_0(\cdot)$ are T -
 585 temperature, μ_B - baryon chemical potential, μ_{I_3} - isospin chemical potential, μ_S
 586 - strange chemical potential, μ_C - charmed chemical potential and the s is a spin of
 587 a particle. The hydrodynamic calculations yield the flow velocity at freeze-out as
 588 well as the stress and bulk viscosity tensors required to calculate non-equilibrium
 589 corrections to the momentum distribution used in Eq. 2.7. The term coming from
 590 shear viscosity has a form [23]

$$\delta f_{shear} = f_0(1 \pm f_0) \frac{1}{2T^2(e + p)} p^\mu p^\nu \pi_{\mu\nu} \quad (2.11)$$

591 and bulk viscosity

$$\delta f_{bulk} = C f_0(1 \pm f_0) \left(\frac{(u^\mu p_\mu)^2}{3u^\mu p_\mu} - c_s^2 u^\mu p_\mu \right) \Pi \quad (2.12)$$

592 where c_s is sound velocity and

$$\frac{1}{C} = \frac{1}{3} \frac{1}{(2\pi)^3} \sum_{hadrons} \int d^3 p \frac{m^2}{E} f_0(1 \pm f_0) \left(\frac{p^2}{3E} - c_s^2 E \right). \quad (2.13)$$

593 2.3 Events generation procedure

594 The equations presented in the previous section are directly used in the
 595 THERMINATOR to generate the primordial hadrons (created during freeze-out)
 596 with the Monte-Carlo method. This procedure consists of 3 main steps, where
 597 the first two are performed only once per given parameter set. After the
 598 generation of primordial particles, the cascade decay of unstable resonances is
 599 performed.

600 Determination of a maximum of an integrand

601 In order to generate particles through a Monte Carlo method, the maximum
 602 value of the distribution in the right-hand-side of Eq. 2.7 must be known. To find
 603 this number, THERMINATOR performs a generation of a sample consisting of a
 604 large number of particles. For each particle the value of a distribution is cal-
 605 culated and the maximum value f_{max} of the sample is stored. A large enough
 606 sample of particles guarantees that f_{max} found in this procedure is a good es-
 607 timate of the maximum value of a distribution in Eq. 2.7. This maximum value
 608 depends on a particle type and values of parameters, but does not change from
 609 event to event, hence this procedure is performed once, at the beginning of the
 610 events generation [18].

611 **Multiplicity calculation**

612 In order to generate events, a multiplicity of each particle must be known.
 613 The multiplicities are obtained through a numerical integration of distribution
 614 functions (Eq. 2.7) in the given integration ranges determined by the model para-
 615 meters. The multiplicities also depend only on the model parameters and they
 616 are also only calculated once at the beginning of the event generation [18].

617 **Events and particles generation**

618 Each of the events produced by THERMINATOR are generated separately. At
 619 first, the multiplicities for each of particle type are generated as random numbers
 620 from a Poisson distribution, with the mean being the average particle multipli-
 621 city determined in the previous step. Then the program proceeds to generate
 622 particles from the heaviest to the lightest particle type. In essence, this procedure
 623 is a generation of the set of six random numbers: three components of particle's
 624 momentum (p_x, p_y, p_z) and three parameters providing space-time coordinates
 625 on a freeze-out hypersurface (ζ, ϕ_s, θ). Event generation procedure is based on
 626 von Neumann's acceptance-rejection algorithm. Firstly, the integrand in Eq. 2.7
 627 is calculated using given set of numbers. Subsequently, a random number from
 628 uniform distribution over $[0; f_{max}]$ is compared to the value of integrand. If it
 629 is lower, then the set of numbers is stored as actual particle. If this condition
 630 was not satisfied, a new set is generated. This procedure is repeated until the
 631 determined number of particles of each kind is generated. At this point all prim-
 632 ordial particles (stable and resonances) have been generated and stored in the
 633 event [18].

634 **Decays of unstable particles**

635 In the next step of event generation, a simulation of decays of unstable res-
 636 onances is performed. A particle is considered as unstable when it has non-zero
 637 width Γ defined in the input files of THERMINATOR. The decays proceed sequen-
 638 tially from the heaviest particles to the lightest. Unstable products of decays are
 639 added to the particles generated in the current event and are processed in the
 640 subsequent steps. If a particle has several decay channels, one of them is selec-
 641 ted randomly with the appropriate probability corresponding to the branching
 642 ratio provided in the input files. THERMINATOR in the hadronic cascade process
 643 performs two-body and three-body decays.

644 At the beginning of the cascade decay, the lifetime τ of a particle with mass
 645 M , moving with the four-momentum p^μ , is generated randomly according to the
 646 exponential decay law $\exp(-\Gamma\tau)$. When the lifetime is known, the point of its
 647 decay is calculated as [18]:

$$x_{decay}^\mu = x_{origin}^\mu + \frac{p^\mu}{M}\tau, \quad (2.14)$$

648 where x_{origin}^μ is a space-time position, where the unstable particle was generated.
 649 At the x_{decay}^μ point decay occurs and daughter particles with energies and mo-
 650 mента determined by the conservation laws are generated. Fig. 2.1 illustrates the
 cascade decay process [18].

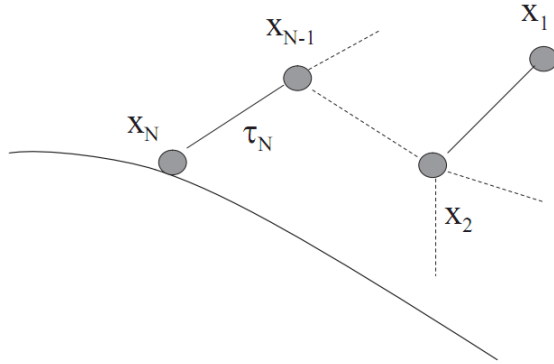


Figure 2.1: The cascade decay in the single freeze-out model. An unstable resonance x_N is formed at the freeze-out hypersurface and travels for the time τ_N depending on its lifetime and decays. If the products are also resonances (x_{N-1} , x_2) they decay further until the stable particles are formed (x_1) [18].

652 **Chapter 3**

653 **Particle interferometry**

654 Two-particle interferometry (also called *femtoscopy*) gives a possibility to
655 investigate space-time characteristics of the particle-emitting source created
656 in heavy ion collisions. Through the study of particle correlations, their
657 momentum distributions can be used to obtain information about the spatial
658 extent of the created system. Using this method, one can measure sizes of the
659 order of 10^{-15} m and time of the order of 10^{-23} s.

660 **3.1 HBT interferometry**

661 In the 1956 Robert Hanbury Brown and Richard Q. Twiss proposed a method
662 which allowed to investigate angular dimensions of stars through analysis of
663 interference between photons. They performed a measurement of the intensity
664 of a beam of light coming from a star using two separated detectors. In a sig-
665 nal plotted as a function of distance between detectors an interference effect was
666 observed, revealing a positive correlation, despite the fact that no phase inform-
667 ation was collected. Hanbury, Brown and Twiss used this interference signal to
668 calculate the angular size of a star with the excellent resolution. This method was
669 designed to be used in astronomy, however HBT interferometry can be used also
670 to measure extent of any emitting source. Therefore it was adapted to heavy ion
671 collisions to investigate dimensions of a particle-emitting source [8].

672 **3.2 Theoretical approach**

673 Intensity interferometry in heavy ion physics uses similar mathematical form-
674 alism as the astronomy HBT measurement. The difference between them is that
675 femtoscopy uses a two-particle relative momentum and yields the space-time
676 picture of a source, whereas the latter method uses the distance between detect-
677 ors to calculate angular size of the star.

678 **3.2.1 Conventions used**

679 In heavy ion collisions to describe particular directions, components of mo-
 680 mentum and location of particles, one uses naming convention called the Bertsch-
 Pratt coordinate system. This system is presented in the Fig. 3.1. The three dir-

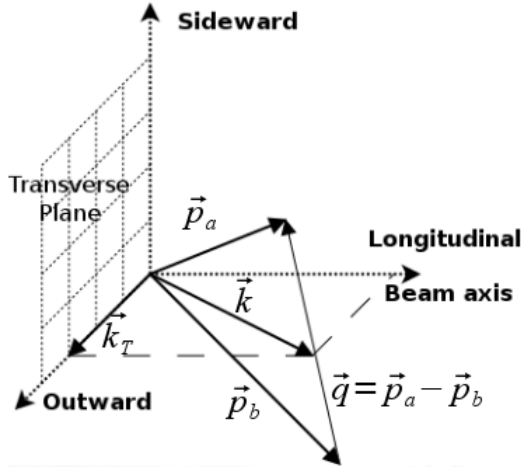


Figure 3.1: Bertsch-Pratt direction naming convention used in heavy ion collision.

681
 682 ections are called *longitudinal*, *outward* and *sideward*. The longitudinal direction
 683 is parallel to the beam axis. The plane perpendicular to the beam axis is called
 684 a *transverse plane*. A projection of a particle pair momentum $\mathbf{k} = (\mathbf{p}_a + \mathbf{p}_b)/2$
 685 on a transverse plane (a *transverse momentum* \mathbf{k}_T) determines *outward* direction:
 686 $(\mathbf{k})_{out} = \mathbf{k}_T$. A direction perpendicular to the longitudinal and outward is called
 687 *sideward*.

688 A particle pair is usually described using two coordinate systems. The first
 689 one, *Longitudinally Co-Moving System* (LCMS) is moving along the particle pair
 690 with the longitudinal direction, in other words, the pair longitudinal momentum
 691 vanishes: $(\mathbf{p}_a)_{long} = -(\mathbf{p}_b)_{long}$. The second system is called *Pair Rest Frame* (PRF).
 692 In the PRF the centre of mass rests: $\mathbf{p}_a = -\mathbf{p}_b$. Variables which are expressed in
 693 the PRF are marked with a star (e.g. \mathbf{k}^*).

The transition of space-time coordinates from LCMS to PRF is simply
 a boost along the outward direction, with the transverse velocity of the
 pair $\beta_T = (\mathbf{v}/c)_{out}$ [26]:

$$r_{out}^* = \gamma_t(r_{out} - \beta_T \Delta t) \quad (3.1)$$

$$r_{side}^* = r_{side} \quad (3.2)$$

$$r_{long}^* = r_{long} \quad (3.3)$$

$$\Delta t^* = \gamma_T(\Delta t - \beta_T r_{out}), \quad (3.4)$$

694 where $\gamma_T = (1 - \beta_T^2)^{-1/2}$ is the Lorentz factor. However, in calculations performed

in this work the equal time approximation is used, which assumes that particles in a pair were produced at the same time in PRF - the Δt^* is neglected.

The most important variables used to describe particle pair are their total momentum $\mathbf{P} = \mathbf{p}_a + \mathbf{p}_b$ and relative momentum $\mathbf{q} = \mathbf{p}_a - \mathbf{p}_b$. In the PRF one has $\mathbf{q} = 2\mathbf{k}^*$, where \mathbf{k}^* is a momentum of the first particle in PRF.

3.2.2 Two particle wave function

Let us consider two identical particles with momenta \mathbf{p}_1 and \mathbf{p}_2 emitted from space points \mathbf{x}_1 and \mathbf{x}_2 . Those emitted particles can be treated as two incoherent waves. If the particles are identical, they are also indistinguishable, therefore one

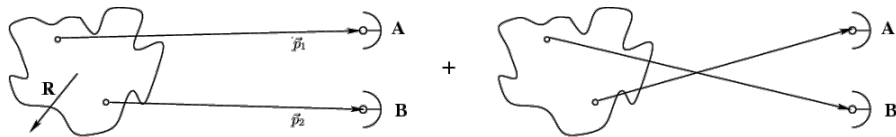


Figure 3.2: The pair wave function is a superposition of all possible states. In case of particle interferometry it includes two cases: particles with momenta p_1, p_2 registered by detectors A, B and p_1, p_2 registered by B, A respectively.

has also take into account the scenario, where the particle with momentum \mathbf{p}_1 is emitted from \mathbf{x}_2 and particle \mathbf{p}_2 from \mathbf{x}_1 (Fig. 3.2). In such case, the wave function describing behaviour of a pair has to contain both components [8]:

$$\Psi_{ab}(\mathbf{q}) = \frac{1}{\sqrt{2}} [\exp(-i\mathbf{p}_1\mathbf{x}_1 - i\mathbf{p}_2\mathbf{x}_2) \pm \exp(-i\mathbf{p}_2\mathbf{x}_1 - i\mathbf{p}_1\mathbf{x}_2)] . \quad (3.5)$$

A two particle wave function of identical bosons is symmetric ("+" sign in Eq. 3.5) and in case of identical fermions - antisymmetric ("−" sign). This anti-symmetrization or symmetrization implies the correlation effect coming from the Fermi-Dirac or Bose-Einstein statistics accordingly.

To provide full description of a system consisting of two charged hadrons, one has to include in the wave function besides quantum statistics also Coulomb and strong Final State Interactions. The aim of this work is an analysis of femtoscopic radii proportional to the inverse of a width of a correlation function (for detailed description see Section 3.2.4). Since we are not interested in the direct comparison of experimental correlation functions with their analytical forms, the following simplification can be made. A width of identical particles correlation function is determined by effects coming from quantum statistics, hence one can ignore influence of Final State Interactions, which in this case is small. Taking into account only quantum statistics can reduce complexity of calculations and save computation time.

722 **3.2.3 Source emission function**

723 To describe particle emitting source, one uses a single emission function [26]:

724

$$S_A(\mathbf{x}_1, \mathbf{p}_1) = \int S(\mathbf{x}_1, \mathbf{p}_1, \mathbf{x}_2, \mathbf{p}_2, \dots, \mathbf{x}_N, \mathbf{p}_N) d\mathbf{x}_2 d\mathbf{p}_2 \dots d\mathbf{x}_N d\mathbf{p}_N \quad (3.6)$$

725 and a two-particle one:

$$S_{AB}(\mathbf{x}_1, \mathbf{p}_1, \mathbf{x}_2, \mathbf{p}_2) = \int S(\mathbf{x}_1, \mathbf{p}_1, \mathbf{x}_2, \mathbf{p}_2, \dots, \mathbf{x}_N, \mathbf{p}_N) d\mathbf{x}_3 d\mathbf{p}_3 \dots d\mathbf{x}_N d\mathbf{p}_N . \quad (3.7)$$

726 Emission function $S(\cdot)$ can be interpreted as a probability to emit a particle, or
 727 a pair of particles from a given space-time point with a given momentum. In
 728 principle, the source emission function should encode all physics aspects of the
 729 particle emission process i.e. the symmetrization for bosons and fermions, as
 730 well as the two-body and many body Final State Interactions. Instead of this,
 731 one assume that each particle's emission process is independent - the interac-
 732 tion between final-state particles after their creation is independent from their
 733 emission process. The assumption of this independence allows to construct two-
 734 particle emission function from single particle emission functions via a convolu-
 735 tion [26]:

$$S(\mathbf{k}^*, \mathbf{r}^*) = \int S_A(\mathbf{p}_1, \mathbf{x}_1) S_B(\mathbf{p}_2, \mathbf{x}_2) \delta \left[\mathbf{k}^* - \frac{\mathbf{p}_1 + \mathbf{p}_2}{2} \right] \delta [\mathbf{r}^* - (\mathbf{x}_1 + \mathbf{x}_2)] \times d^4 \mathbf{x}_1 d^4 \mathbf{x}_2 d^4 \mathbf{x}_1 d^3 \mathbf{p}_1 d^3 \mathbf{p}_2 \quad (3.8)$$

736 In case of identical particles, ($S_A = S_B$) several simplifications can be made. A
 737 convolution of the two identical Gaussian distributions is also a Gaussian distri-
 738 bution with σ multiplied by $\sqrt{2}$. Femtoscopy can give information only about
 739 two-particle emission function, but when considering Gaussian distribution as
 740 a source function in Eq. 3.8, one can obtain a σ of a single emission function
 741 from a two-particle emission function. The Eq. 3.8 is not reversible - an inform-
 742 ation about $S_A(\cdot)$ cannot be derived from $S_{AB}(\cdot)$. An exception from this rule
 743 is a Gaussian source function, hence it is often used in femtoscopic calculations.
 744 Considering pairs of identical particles, an emission function is assumed to be
 745 described by the following equation in the Pair Rest Frame [26]:

$$S_{1D}^{PRF}(\mathbf{r}^*) = \exp \left(-\frac{r_{out}^{*2} + r_{side}^{*2} + r_{long}^{*2}}{4R_{inv}^2} \right) . \quad (3.9)$$

To change from the three-dimensional variables to the one-dimensional variable
 one requires introduction of the proper Jacobian r^{*2} .

$$S_{1D}^{PRF}(r^*) = r^{*2} \exp \left(-\frac{r^{*2}}{4R_{inv}^2} \right) . \quad (3.10)$$

746 The “4” in the denominator before the “standard deviation” R_{inv} in the Gaussian
 747 distribution comes from the convolution of the two Gaussian distributions,
 748 which multiplies the R_{inv} by a factor of $\sqrt{2}$.

A more complex form of emission function was used by all RHIC and SPS experiments in identical pion femtoscopy:

$$S_{3D}^{LCMS}(\mathbf{r}) = \exp \left(-\frac{r_{out}^2}{4R_{out}^2} - \frac{r_{side}^2}{4R_{side}^2} - \frac{r_{long}^2}{4R_{long}^2} \right). \quad (3.11)$$

749 The main difference of this source function is that it has three different and inde-
 750 pendent widths R_{out} , R_{side} , R_{long} and they are defined in the LCMS, not in PRF.
 751 Unlike in PRF, in LCMS an equal-time approximation is not used. For identical
 752 particles this is not a problem - only Coulomb interaction inside a wave function
 753 depends on Δt .

754 Relationship between one-dimensional and three-dimensional source sizes

755 Up to now, most of femtoscopic measurements were limited only to averaged
 756 source size R_{av}^L (the letter “L” in superscript stands for LCMS):

$$S_{1D}^{LCMS}(\mathbf{r}) = \exp \left(-\frac{r_{out}^2 + r_{side}^2 + r_{long}^2}{2R_{av}^L} \right). \quad (3.12)$$

757 The relationship between between $S_{1D}^{LCMS}(\cdot)$ and $S_{3D}^{LCMS}(\cdot)$ is given by:

$$S_{3D}^{LCMS}(r) = \int \exp \left(-\frac{r_{out}^2}{2R_{out}^L} - \frac{r_{side}^2}{2R_{side}^L} - \frac{r_{long}^2}{2R_{long}^L} \right) \times \delta \left(r - \sqrt{r_{out}^2 + r_{side}^2 + r_{long}^2} \right) dr_{out} dr_{side} dr_{long}. \quad (3.13)$$

758 The one-dimensional source size corresponding to the three-dimensional one can
 759 be approximated by the following form:

$$S_{1D}^{LCMS}(r) = r^2 \exp \left(-\frac{r^2}{2R_{av}^L} \right). \quad (3.14)$$

760 The equation above assumes that $R_{out}^L = R_{side}^L = R_{long}^L$ hence $R_{av}^L = R_{out}^L$. If this
 761 condition is not satisfied, one can not give explicit mathematical relation between
 762 one-dimensional and three-dimensional source sizes. However, for realistic val-
 763 ues of R (i.e. for similar values of R_{out} , R_{side} , R_{long}), the S_{3D}^{LCMS} from Eq. 3.13 is
 764 not very different from Gaussian distribution and can be well approximated by
 765 Eq. 3.13.

766 A deformation of an averaged source function in case of big differences in
 767 R_{out} , R_{side} , R_{long} is presented in the Fig. 3.3. A three-dimensional Gaussian dis-
 768 tribution with varying widths was averaged into one-dimensional function using

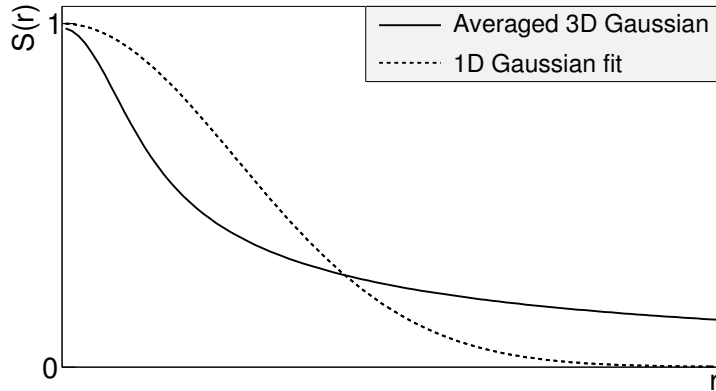


Figure 3.3: An averaged three-dimensional Gaussian source function with different widths was averaged into one-dimensional function. To illustrate deformations, one-dimensional Gaussian distribution was fitted.

the Eq. 3.13. Afterwards, an one-dimensional Gaussian distribution was fitted.
 One can notice a heavy tail of an averaged distribution in long r region, which
 makes an approximation using one-dimensional distribution in this case quite
 inaccurate.

Using Eq. 3.13 and Eq. 3.14 one can obtain a relation between one-dimensional width and the three-dimensional ones. Through numerical calculations one can find the following approximate relation [26]:

$$R_{av}^L = \sqrt{\left(R_{out}^{L^2} + R_{side}^{L^2} + R_{long}^{L^2}\right)/3}. \quad (3.15)$$

This equation does not depend on the pair velocity, hence it is valid in the LCMS and PRF.

3.2.4 Analytical form of a correlation function

The fundamental object in a particle interferometry is a correlation function.
 The correlation function is defined as:

$$C(\mathbf{p}_a, \mathbf{p}_b) = \frac{P_2(\mathbf{p}_a, \mathbf{p}_b)}{P_1(\mathbf{p}_a)P_1(\mathbf{p}_b)}, \quad (3.16)$$

where P_2 is a conditional probability to observe a particle with momentum \mathbf{p}_b if particle with momentum \mathbf{p}_a was also observed. A P_1 is a probability to observe a particle with a given momentum. The relationship between source emission function, pair wave function and the correlation function is described by the following equation:

$$C(\mathbf{p}_1, \mathbf{p}_2) = \int S_{AB}(\mathbf{p}_1, \mathbf{x}_1, \mathbf{p}_2, \mathbf{x}_2) |\Psi_{AB}|^2 d^4\mathbf{x}_1 d^4\mathbf{x}_2 \quad (3.17)$$

Substituting the one-dimensional emission function (Eq. 3.10) into the integral above yields the following form of correlation function in PRF:

$$C(q) = 1 + \lambda \exp(-R_{inv}^2 q^2) \quad (3.18)$$

where q is a momentum difference between two particles. When using the three-dimensional emission function (Eq. 3.11) one gets the following correlation function defined in the LCMS:

$$C(\mathbf{q}) = 1 + \lambda \exp(-R_{out}^2 q_{out}^2 - R_{side}^2 q_{side}^2 - R_{long}^2 q_{long}^2) \quad (3.19)$$

where q_{out} , q_{side} , q_{long} are \mathbf{q} components in the outward, sideward and longitudinal direction. The λ parameter in the equations above determines correlation strength. The lambda parameter has values in the range $\lambda \in [-0.5, 1]$ and it depends on a pair type. In case of pairs of identical bosons (like $\pi\pi$ or KK) the lambda parameter $\lambda \rightarrow 1$. For identical fermions (e.g. $p-p$) $\lambda \rightarrow -0.5$. Values of λ observed experimentally are lower than 1 (for bosons) and greater than -0.5 (for fermions). There are few explanations to this effect: detector efficiencies, inclusion of misidentified particles in a used sample or inclusion of non-correlated pairs (when one or both particles come from e.g. long-lived resonance). The analysis carried out in this work uses data from a model, therefore the detector efficiency and particle purity is not taken into account [26].

3.2.5 Spherical harmonics decomposition of a correlation function

Results coming from an analysis using three-dimensional correlation function in Cartesian coordinates are quite difficult to visualize. To do that, one usually performs a projection into one dimension in outward, sideward and longitudinal directions. One may loose important information about a correlation function in this procedure, because it gives only a limited view of the full three-dimensional structure. Recently, a more advanced way of presenting correlation function - a spherical harmonics decomposition, was proposed. The three-dimensional correlation function is decomposed into an infinite set of components in a form of one-dimensional histograms $C_l^m(q)$. In this form, a correlation function is defined as a sum of a series [27]:

$$C(\mathbf{q}) = \sum_{l,m} C_l^m(q) Y_l^m(\theta, \phi), \quad (3.20)$$

where $Y_l^m(\theta, \phi)$ is a spherical harmonic function. Spherical harmonics are an orthogonal set of solutions to the Laplace's equation in spherical coordinates. Hence, in this approach, a correlation function is defined as a function of q , θ and ϕ . To obtain C_l^m coefficients in the series, one has to calculate the following integral:

$$C_l^m(q) = \int_{\Omega} C(q, \theta, \phi) Y_l^{m*}(\theta, \phi) d\Omega, \quad (3.21)$$

810 where Ω is a full solid angle.

Spherical harmonics representation has several important advantages. The main one is that it requires less statistics than traditional analysis performed in Cartesian coordinates. Another one is that it encodes full three-dimensional information in a set of one-dimensional plots. In principle it does not have to be an advantage, because full description of a correlation function requires infinite number of l, m components. But it so happens that the intrinsic symmetries of a pair distribution in a femtoscopic analysis result in most of the components to vanish. For the identical particles correlation functions, all coefficients with odd values of l and m disappear. It has also been shown, that the most significant portion of femtoscopic data is stored in the components with the lowest l values. It is expected that, the main femtoscopic information is contained in the following components [26]:

$$C_0^0 \rightarrow R_{LCMS}, \quad (3.22)$$

$$\Re C_2^0 \rightarrow \frac{R_T}{R_{long}}, \quad (3.23)$$

$$\Re C_2^2 \rightarrow \frac{R_{out}}{R_{side}}, \quad (3.24)$$

811 where $R_{LCMS} = \sqrt{(R_{out}^2 + R_{side}^2 + R_{long}^2)/3}$ and $R_T = \sqrt{(R_{out}^2 + R_{side}^2)/2}$.

812 The C_0^0 is sensitive to the overall size of a correlation function. The $\Re C_2^0$ carries
 813 the information about the ratio of the transverse to the longitudinal radii, due
 814 to its $\cos^2(\theta)$ weighting in Y_2^0 . The component $\Re C_2^2$ with its $\cos^2(\phi)$ weighting
 815 encodes the ratio between outward and sideward radii. Thus, the spherical har-
 816 monics method allows to obtain and analyze full three-dimensional femtoscopic
 817 information from a correlation function [26].

818 3.3 Experimental approach

819 The correlation function is defined as a probability to observe two particles
 820 together divided by the product of probabilities to observe each of them sepa-
 821 rately (Eq. 3.16). Experimentally this is achieved by dividing two distributions
 822 of relative momentum of pairs of particles coming from the same event and the
 823 equivalent distribution of pairs where each particle is taken from different colli-
 824 sions. In this way, one obtains not only femtoscopic information but also all other
 825 event-wide correlations. This method is useful for experimentalists to estimate
 826 the magnitude of non-femtoscopic effects. There exists also a different approach,
 827 where two particles in pairs in the second distribution are also taken from the
 828 same event. The second method gives only information about physical effects
 829 accessible via femtoscopy. The aim of this work is a study of effects coming from
 830 two particle interferometry, hence the latter method was used.

831 In order to calculate experimental correlation function, one uses the follow-
 832 ing approach. One has to construct two histograms: the *numerator* N and the

833 denominator D with the particle pairs momenta, where particles are coming from
 834 the same event. Those histograms can be one-dimensional (as a function of $|\mathbf{q}|$),
 835 three dimensional (a function of three components of \mathbf{q} in LCMS) or a set of one-
 836 dimensional histogram representing components of the spherical harmonic de-
 837 composition of the distribution. The second histogram, D is filled for each pair
 838 with the weight 1.0 at a corresponding relative momentum $\mathbf{q} = 2\mathbf{k}^*$. The first one,
 839 N is filled with the same procedure, but the weight is calculated as $|\Psi_{ab}(\mathbf{r}^*, \mathbf{k}^*)|^2$.
 840 A division N/D gives the correlation function C . This procedure can be simply
 841 written as [26]:

$$C(\mathbf{k}^*) = \frac{N}{D} = \frac{\sum_{n_i \in D} \delta(\mathbf{k}_i^* - \mathbf{k}^*) |\Psi_{ab}(\mathbf{r}_i^*, \mathbf{k}_i^*)|^2}{\sum_{n_i \in D} \delta(\mathbf{k}_i^* - \mathbf{k}^*)} . \quad (3.25)$$

The D histogram represents the set of all particle pairs used in calculations.
 The n_i is a pair with the its relative momentum \mathbf{k}_i^* and relative separation \mathbf{r}_i^* .
 Mathematically, the procedure of calculating the Eq. 3.25 is equivalent to a
 calculation of an integral in Eq. 3.17 through a Monte-Carlo method. The wave
 function used in Eq. 3.25 has one of the following forms:

$$|\Psi_{\pi\pi}(\mathbf{r}^*, \mathbf{k}^*)|^2 = |\Psi_{KK}(\mathbf{r}^*, \mathbf{k}^*)|^2 = 1 + \cos(2\mathbf{k}^* \mathbf{r}^*) , \quad (3.26)$$

$$|\Psi_{pp}(\mathbf{r}^*, \mathbf{k}^*)|^2 = 1 - \frac{1}{2} \cos(2\mathbf{k}^* \mathbf{r}^*) . \quad (3.27)$$

842 The first one is used in case of bosons, and the latter one is for identical fermions.
 843 A wave function for pair of spin-1/2 fermions (Eq. 3.27) is a superposition of two
 844 possible states: singlet state (with spin equal to 0 and one eigenstate) and triplet
 845 state (with spin equal to 1 and three possible eigenstates). For a singlet state, a
 846 wave function is symmetric, and for triplet state, it is antisymmetric. In other
 847 words the $|\Psi_{pp}|^2$ encodes correlation coming from Bose-Einstein statistics (with
 848 weight 1/4) and anti-correlation from Fermi-Dirac distribution (with weight 3/4).

849 3.4 Scaling of femtoscopy radii

850 A particle interferometry formalism presented in the previous sections as-
 851 sumes that particle emitting source is static. This is not the case in heavy ion
 852 collisions at LHC. An existence of transverse radial and elliptic flow suggest that
 853 created system is dynamic. To address this issue, a concept of *lengths of homogen-*
 854 *eity* was introduced. It is defined as:

$$\frac{|f(p, x + \lambda) - f(p, x)|}{f(p, x)} = 1 , \quad (3.28)$$

855 where λ is the homogeneity length. It can be interpreted as the distance at which
 856 relative change of the source Wigner function f becomes large. One can measure

the lengths of homogeneity of a system using femtoscopic radii. This concept can be intuitively explained on a basis of hydrodynamic models. Each source element is emitting particles with a velocity which is a combination of two components: a fluid cell velocity β_f (which is taken from the flow field $u_\mu(x^\mu)$) and thermal velocity β_{th} (which has random direction). These particles can combine into pairs of small relative momenta and become correlated. If two particles are emitted far ($|x_a - x_b| > \lambda$) away from each other, the flow field u_μ in their point of emission might be very different and it will be impossible for them to have sufficiently small relative momenta to be in the region of interference effect. This effect is presented in Fig. 3.4. An increase of a correlation is visible for pairs with low relative momenta [8].

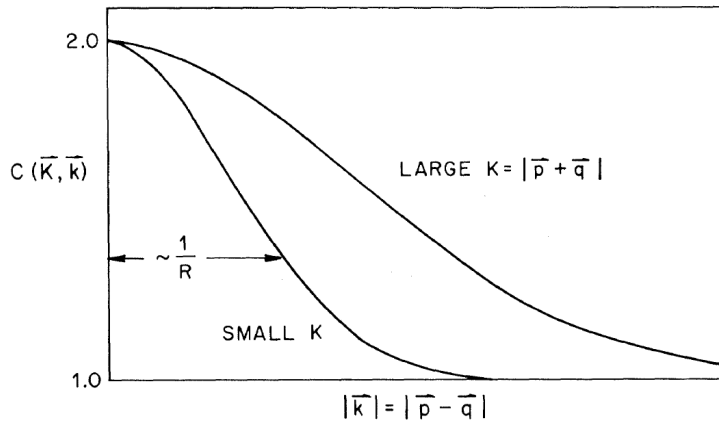


Figure 3.4: Correlation function width dependence on total pair momentum. Pion pairs with a large total momentum have a wider correlation (smaller apparent source) [28].

867

868 3.4.1 Scaling in LCMS

Hydrodynamic calculations performed in LCMS show that femtoscopic radii in outward, sideward, and longitudinal direction show dependence on transverse mass $m_T = \sqrt{k_T^2 + m^2}$, where m is a mass of a particle [29]. Moreover, experimental results show that this scaling is observed for R_{LCMS} radii also. This dependence can be expressed as follows:

$$R_i = \alpha m_T^{-\beta} \quad (3.29)$$

869 where i subscript indicates that this equation applies to R_{out} , R_{side} and R_{long}
870 radii. The β exponent is approximately equal 0.5. In case of strong transversal
871 expansion of the emitting source, the decrease of longitudinal interferometry ra-
872 dius can be more quick than $m_T^{-0.5}$, hence one can expect for longitudinal radii
873 greater values of $\beta > 0.5$ [29].

874 **3.4.2 Scaling in PRF**

875 In the collisions at the LHC energies, pions are most abundant particles and
 876 their multiplicities are large enough to enable three-dimensional analysis. How-
 877 ever, for heavier particles, such as kaons and protons statistical limitations arise.
 878 Hence it is often possible to only measure one-dimensional direction-averaged
 879 radius R_{inv} for those particles. The R_{inv} is then calculated in the PRF. The trans-
 880 ition from LCMS to PRF is a Lorentz boost in the direction of pair transverse
 881 momentum with velocity $\beta_T = p_T/m_T$. Hence only R_{out} changes:

$$R_{out}^* = \gamma_T R_{out}. \quad (3.30)$$

882 A Lorentz factor $\gamma_T = m_T/m$ depends on the particle type, therefore for the
 883 lighter particles (and for the same m_T) γ_T is much larger, which causes bigger
 884 growth of R_{out} and overall radius. This transformation to PRF breaks the scaling
 885 observed in the LCMS radii.

886 This increase of radius in the outward direction induces overall source
 887 size growth and whatsoever the source distribution function becomes
 888 non-gaussian. In this case the source function is developing long-range tails and
 889 its one-dimensional projection is much narrower than Gaussian distribution.
 890 This deformation is presented in Fig. 3.3. The influence of these effects can be
 891 expressed with an approximate formula:

$$R_{inv} = \sqrt{(R_{out}^2 \sqrt{\gamma_T} + R_{side}^2 + R_{long}^2)/3}. \quad (3.31)$$

892 Because the averaging of the radii is done in quadrature, one would have expec-
 893 ted appearance of γ_T^2 instead of $\sqrt{\gamma_T}$ in this equation. However the Monte-Carlo
 894 procedure shows that this is not the case and the actual growth is smaller than
 895 the naive expectation. Numerical simulations yield that this increase is best de-
 896 scribed with the $\sqrt{\gamma_T}$ in the Eq. 3.31 [30].

Assuming that radii in all directions are equal $R_{out} = R_{side} = R_{long}$, Eq. 3.31
 can be reverted using Eq. 3.15 to express relationship between LCMS and PRF
 overall radii [30]:

$$R_{LCMS} \approx R_{inv} \times [(\sqrt{\gamma_T} + 2)/3]^{-1/2}. \quad (3.32)$$

897 This approximate formula allows to restore power-law behaviour of the scaled
 898 radii not only when the radii are equal, but also when their differences are small
 899 (for explanation see the last part of the Section 3.2.3).

900 This method of recovering scaling in PRF can be used as a tool for the search
 901 of hydrodynamic collectivity between pions, kaons and protons in heavy ion col-
 902 lisions with the measurement of one-dimensional radius in PRF.

903 **Chapter 4**

904 **Results**

905 For the purposes of the femtosopic analysis in this thesis, the THERMINATOR
906 model was used to generate large number of events for eight different sets of
907 initial conditions corresponding the following centrality ranges: 0-5%, 0-10%,
908 10-20%, 20-30%, 30-40%, 40-50%, 50-60% and 60-70% for the Pb-Pb collisions at
909 the centre of mass energy $\sqrt{s_{NN}} = 2.76$ TeV. Software used in the process of
910 calculating correlation functions is described in Appendix A. Plots in this chapter
911 were generated using macros described in Appendix C.

912 **4.1 Identical particles correlations**

913 The correlation functions (three-dimensional and one-dimensional) were cal-
914 culated separately for the following different pairs of identical particles: π - π , K -
915 K and p - p for nine k_T bins (in GeV/c): 0.1-0.2, 0.2-0.3, 0.3-0.4, 0.4-0.5, 0.6-0.7,
916 0.7-0.8, 0.8-1.0 and 1.0-1.2. In case of kaons, k_T ranges start from 0.3 and for pro-
917 tons from 0.4 and for both of them the maximum value is 1.0. The k_T ranges for
918 the heavier particles were limited to maintain sufficient multiplicity to perform
919 reliable calculations.

920 **4.1.1 Spherical harmonics components**

921 The three-dimensional correlation function as a function of relative
922 momentum q_{LCMS} was calculated in a form of components of spherical
923 harmonics series accordingly to the Eq. 3.21. In the femtosopic analysis of
924 identical particles, the most important information is stored in the $\Re C_0^0$, $\Re C_2^0$
925 and $\Re C_2^2$, hence only those components were analyzed. Correlation functions
926 obtained in this procedure were calculated for the different centrality bins for the
927 pairs of pions, kaons and protons. They are presented in the Fig. 4.1, 4.2 and 4.3.

928 Coefficients for pairs of identical bosons (pions and kaons) are shown
929 in the Fig. 4.1 and 4.2. The wave function symmetrization (Bose-Einstein
930 statistics) causes the increase of a correlation in the low relative momenta

regime ($q_{LCMS} < 0.06 \text{ GeV/c}$ or even $q_{LCMS} < 0.12 \text{ GeV/c}$ for more peripheral collisions). It is clearly visible in the $\Re C_0^0$ component. The $\Re C_0^0$ resembles one-dimensional correlation function and in the sense that it encodes information about the overall source radius. The second coefficient $\Re C_2^0$ differs from zero (is negative), which yields the information about the ratio R_T/R_{long} . The $\Re C_2^2$ stores the information about R_{out}/R_{side} ratio and one can notice that it is non-vanishing (is also negative).

The correlation function for a pair of identical fermions is presented in the Fig. 4.3. A wave function for a pair of protons is a composition of singlet (described by Bose-Einstein statistics) and triplet state (described by the

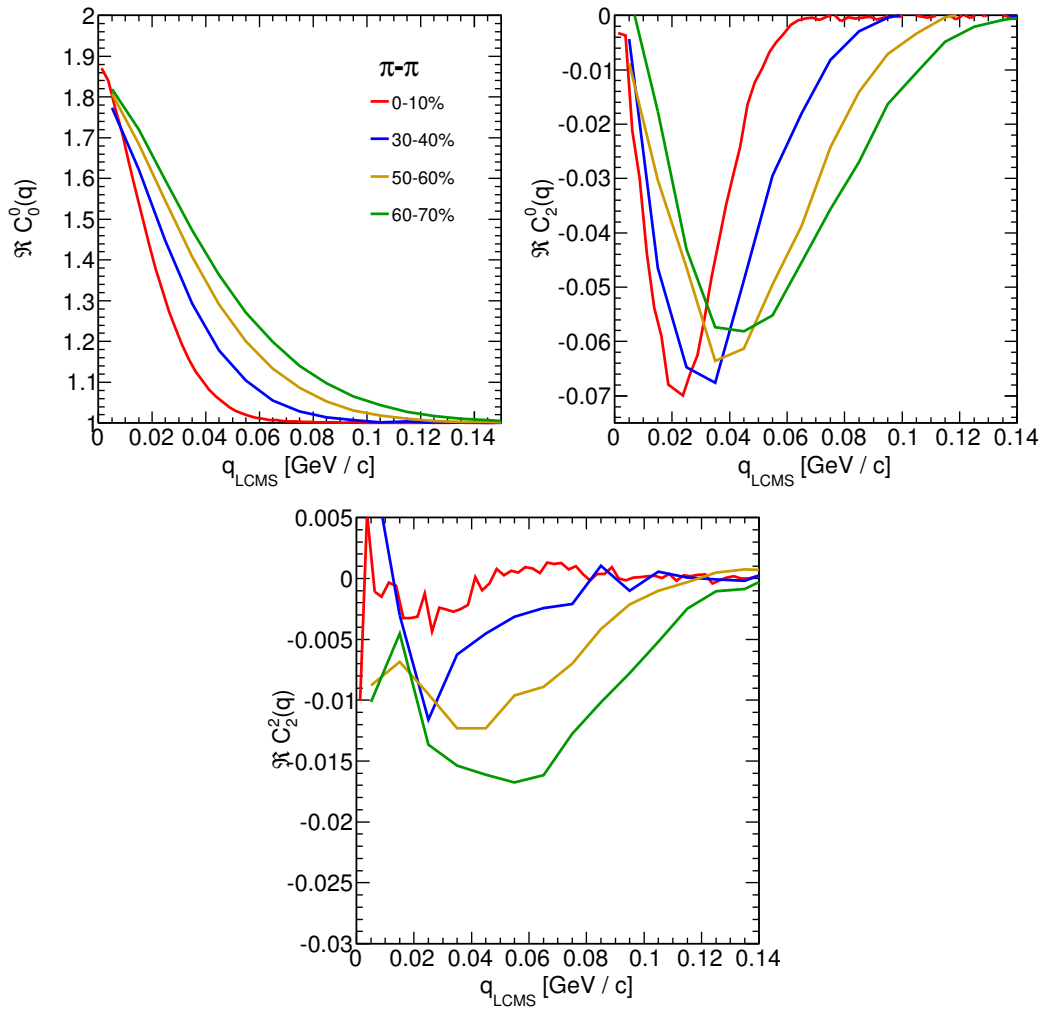


Figure 4.1: Spherical harmonics coefficients of the two-pion correlation function. From the top left: $\Re C_0^0$, $\Re C_2^0$ and $\Re C_2^2$. Only few centrality bins are presented for increased readability.

941 Fermi-Dirac statistics - see Section 3.3). An influence of Fermi-Dirac statistics has
 942 its effect in the decrease of a correlation down to 0.5 at low relative momentum
 943 ($q_{LCMS} < 0.1 \text{ GeV/c}$ or $q_{LCMS} < 0.15 \text{ GeV/c}$ for more peripheral collisions),
 944 which can be observed in $\Re C_0^0$. The $\Re C_2^0$ and $\Re C_2^2$ coefficients differ from zero
 945 and are becoming positive.

946 The common effect of the spherical harmonics form of a correlation function
 947 is the “mirroring” of the shape of the $\Re C_0^0$ coefficient - when correlation func-
 948 tion increases at low q_{LCMS} , the $\Re C_2^0$ and $\Re C_2^2$ are becoming negative and vice
 949 versa. This is quite different behaviour than in the case of correlations of non-

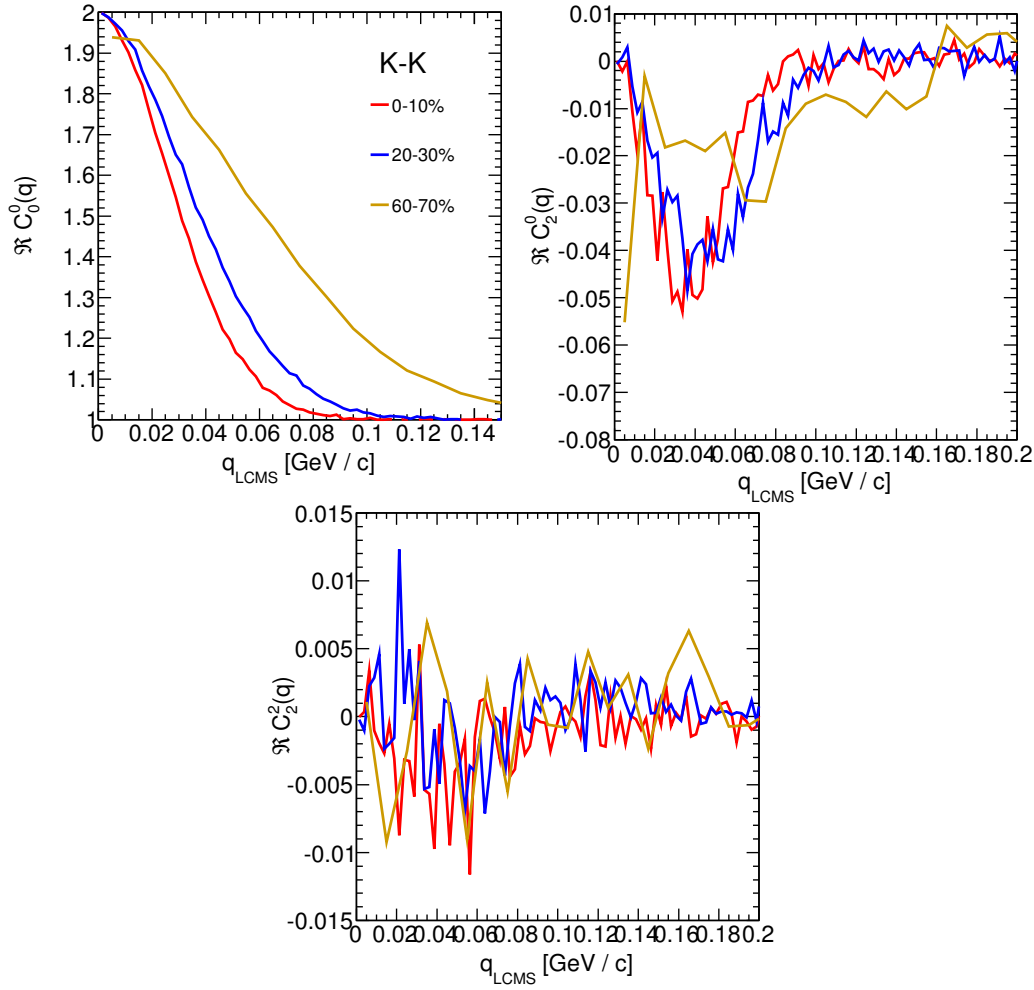


Figure 4.2: Spherical harmonics coefficients of the two-kaon correlation function. From the top left: $\Re C_0^0$, $\Re C_2^0$ and $\Re C_2^2$. Only few centrality bins are presented for increased readability. The $\Re C_2^2$ is noisy, but one can still notice that it differs from zero and is becoming negative.

950 identical particles, where the $\Re C_2^0$ still behaves in the same manner, but $\Re C_2^2$ has
 951 the opposite sign to the $\Re C_2^0$ [26].

952 In all cases, the correlation function gets wider with the peripherality of a
 953 collision i.e. the correlation function for most central collisions (0-10%) is much
 954 narrower than for the most peripheral ones (60-70%). This phenomena is clearly
 955 visible the $\Re C_0^0$ coefficients. Other components are also affected by this effect,
 956 this is especially noticeable in the case of kaons and pions. For the protons, the
 957 results are noisy, hence this effect is not clearly distinguishable.

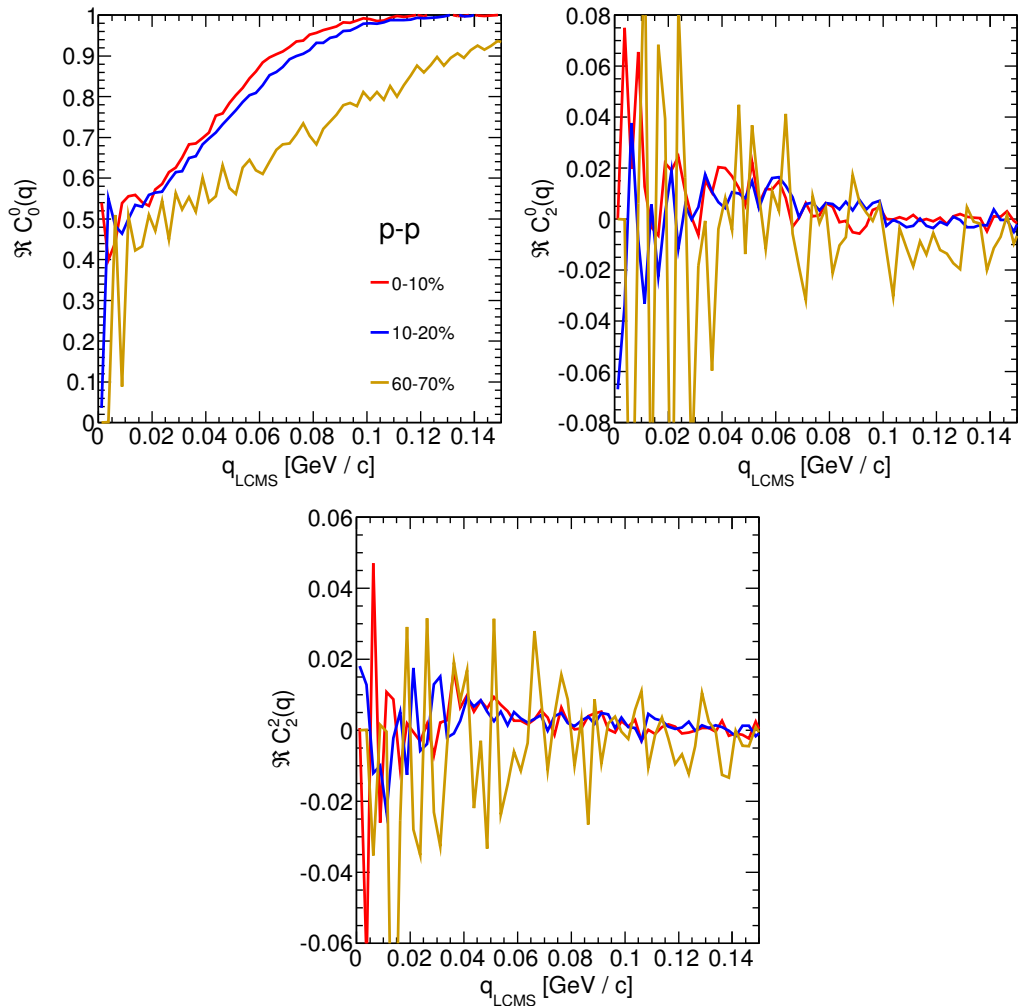


Figure 4.3: Spherical harmonics coefficients of the two-proton correlation function. From the top left: $\Re C_0^0$, $\Re C_2^0$ and $\Re C_2^2$. Only few centrality bins are presented for increased readability. The $\Re C_2^0$ and $\Re C_2^2$ are noisy, but one can still notice, that they differ from zero and are becoming positive.

958 **4.1.2 Centrality dependence of a correlation function**

959 The centrality dependence of a correlation function is especially visible in
960 one-dimensional correlation functions. This effect is presented in the Fig. 4.4 -
961 the correlation functions for pions, kaons and protons are plotted for the same
962 k_T range but different centrality bins. One can notice that the width of a func-
963 tion is smaller in the case of most central collisions. Hence, the femtoscopic radii
964 (proportional to the inverse of width) are increasing with the centrality. An ex-
965 planation for this growth is that in the most central collisions, a size of a created
system is larger than for the peripheral ones.

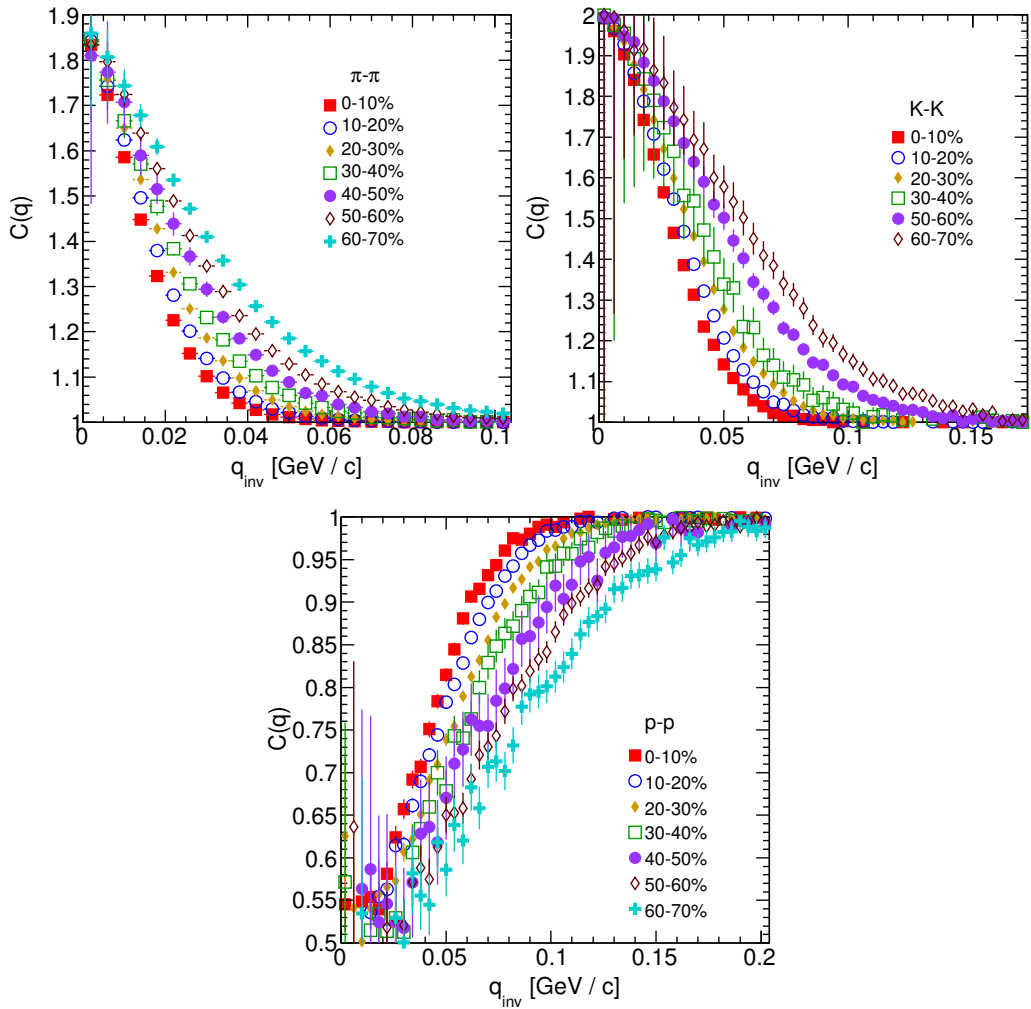


Figure 4.4: One-dimensional correlation function for pions (top left), kaons (top right) and protons (bottom) for different centralities.

4.1.3 k_T dependence of a correlation function

In the Fig. 4.5 there are presented one-dimensional correlation functions for pions, kaons and protons for the same centrality bin, but different k_T ranges. One can observe in all cases of the particle types, appearance of the same trend: with the increase of the total transverse momentum of a pair, the width of a correlation function increases and the femtoscopic radius decreases. The plots in the Fig. 4.5 were zoomed in to show the influence of k_T .

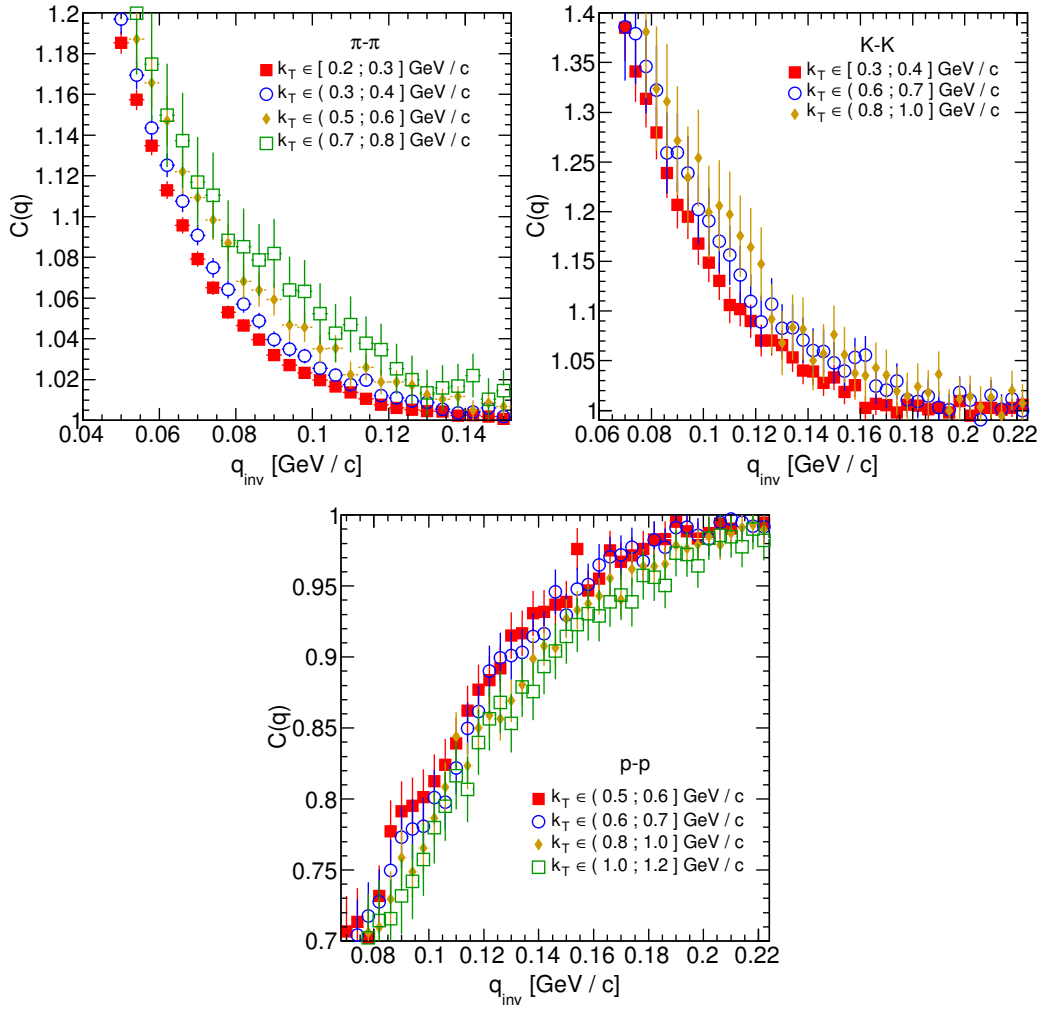


Figure 4.5: One-dimensional correlation functions for pions, kaons and protons, for the same centrality bin and different k_T ranges. The plot was zoomed in to the region which illustrates the k_T dependence in the best way. Only few of the calculated ranges are presented for better readability.

974 4.2 Results of the fitting procedure

975 In order to perform a quantitative analysis of a wide range of correlation
 976 functions, the theoretical formulas were fitted to the calculated experimental-
 977 like data. In this procedure, the femtoscopic radii for the three-dimensional as
 978 well as one-dimensional correlation functions were extracted. The main goal of
 979 this analysis is a verification of a common transverse mass scaling for different
 980 particles types. Obtained radii are plotted as a function of a transverse mass
 981 $m_T = \sqrt{k_T^2 + m^2}$. To test the scaling, the following power-law was fitted to the
 982 particular radii afterwards:

$$R_x = \alpha m_T^{-\beta}, \quad (4.1)$$

983 where the α and β are free parameters. The procedure of fitting and used soft-
 984 ware are described in Appendix B.

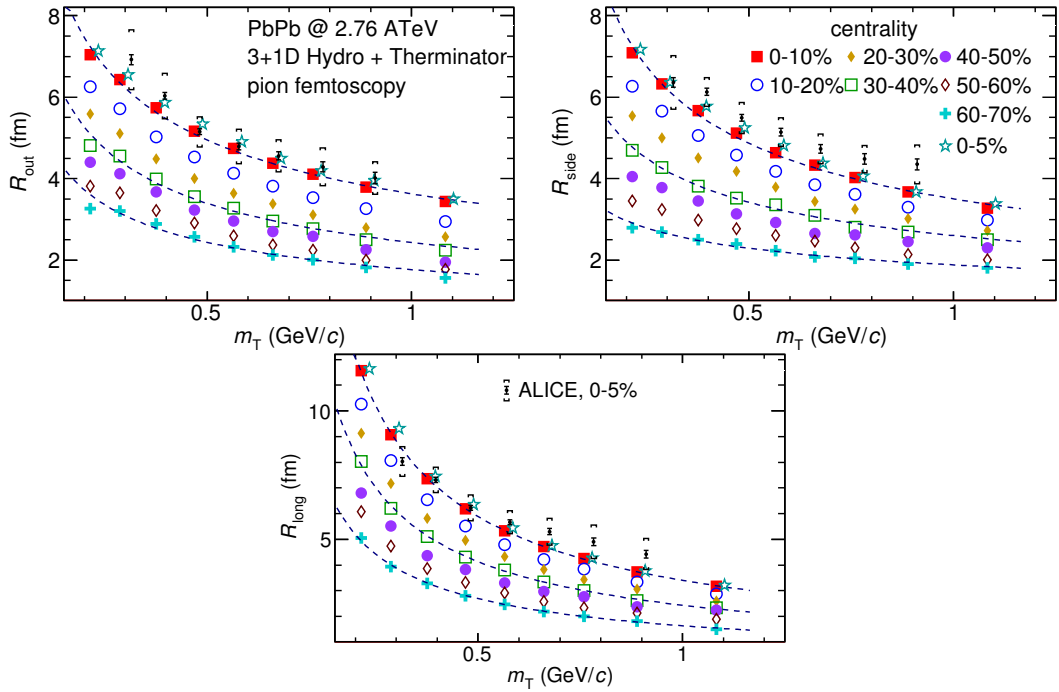


Figure 4.6: Femtoscopic radii in LCMS coming from two-pion correlation functions for all centrality bins as a function of m_T . The dashed lines are power-law fits. The most central collisions (0-5%) are compared to the results from ALICE [31]. The two datasets are shifted to the right for visibility [30].

4.2.1 The three-dimensional femtoscopic radii scaling

The femtoscopic radii in the outward, sideward and longitudinal directions for the analysis of two-pion correlation functions in the LCMS are presented in Fig. 4.6. The dashed lines are fits of the power law to the data. One can notice, that the power law describes data points well with a 5% accuracy. The β fit parameter for the outward direction is in the order of 0.45. For the sideward direction, this parameter has the similar value, but it is lower for the most peripheral collisions. In case of the longitudinal direction, the β has greater value, up to 0.75. In the Fig. 4.6, results for the top 5% central collisions (star-shaped markers) with experimental data from ALICE [31] are also compared. The experimental results are consistent with the ones coming from the model predictions.

The Fig. 4.7 presents femtoscopic radii coming from the kaon calculations. The R_{out} , R_{side} and R_{long} fall also with the power-law within the 5% accuracy. The β parameter was larger in case of kaons: 0.59 in outward direction, 0.54 in the sideward and 0.86 for longitudinal.

The results for two-proton analysis are shown in the Fig. 4.8. The Eq. 4.1 was fitted to the data and tells that the protons also follow the m_T scaling within 5% range. The β parameter values were even bigger for the outward (0.58),

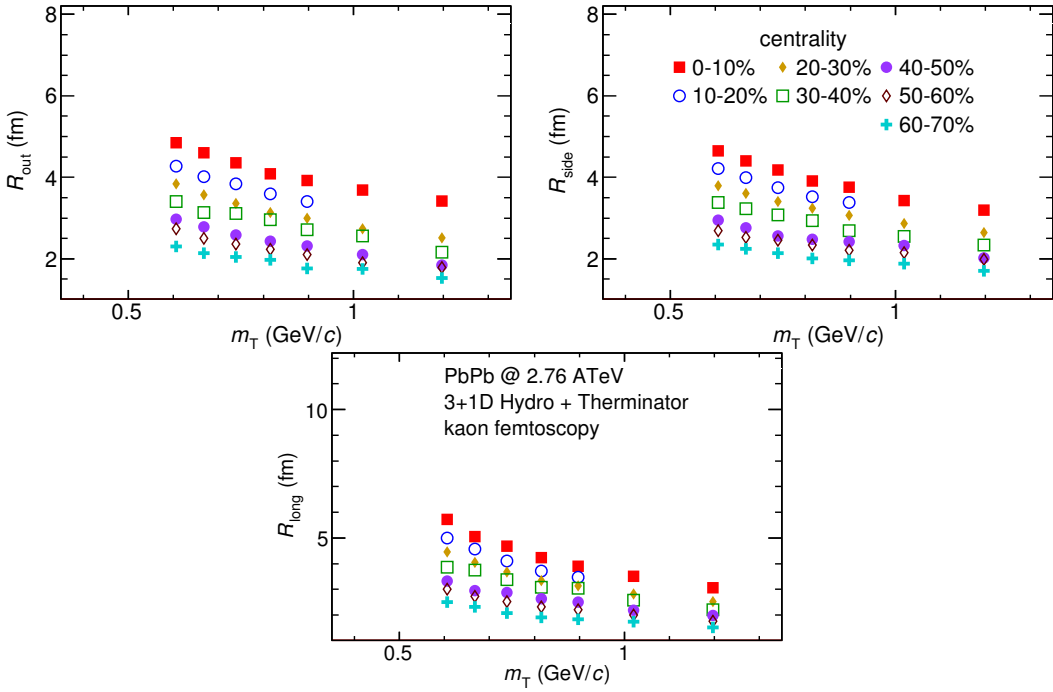


Figure 4.7: Femtoscopic radii extracted from two-kaon correlation functions for different centrality bins as a function of m_T . [30].

1004 sideward (0.61) and longitudinal (1.09) directions than for the other particle
 1005 types.

1006 The Fig. 4.9 presents results for the pions, kaons and protons together as a
 1007 function of m_T . Considering differences in the β value for the fits for differ-
 1008 ent particles, one can suspect that there is no common scaling between different
 1009 kinds of particles. However, when all of the results shown on the same plot, they
 1010 are aligning on the common curve and the scaling is well preserved. The scaling
 1011 accuracy is 3%, 5% and 4% for the 0-10%, 20-30% and 60-70% for the outward
 1012 direction. For the sideward radii the scaling is better, with average deviations
 1013 2%, 2% and 3% respectively. In case of longitudinal direction the accuracy is 6%,
 1014 5% and 3% for the three centralities. The β parameter for the outward direction is
 1015 close to 0.42 in all cases. For the sideward direction it varies from 0.28 to 0.47 and
 1016 is bigger for more central collisions. Regarding longitudinal radii, the exponent
 1017 is bigger than the other two: $\beta \in [0.62; 0.72]$. Considering all results, the plotted
 1018 radii are following the common power-law scaling within the 5% accuracy for all
 1019 directions, centralities and particle types.

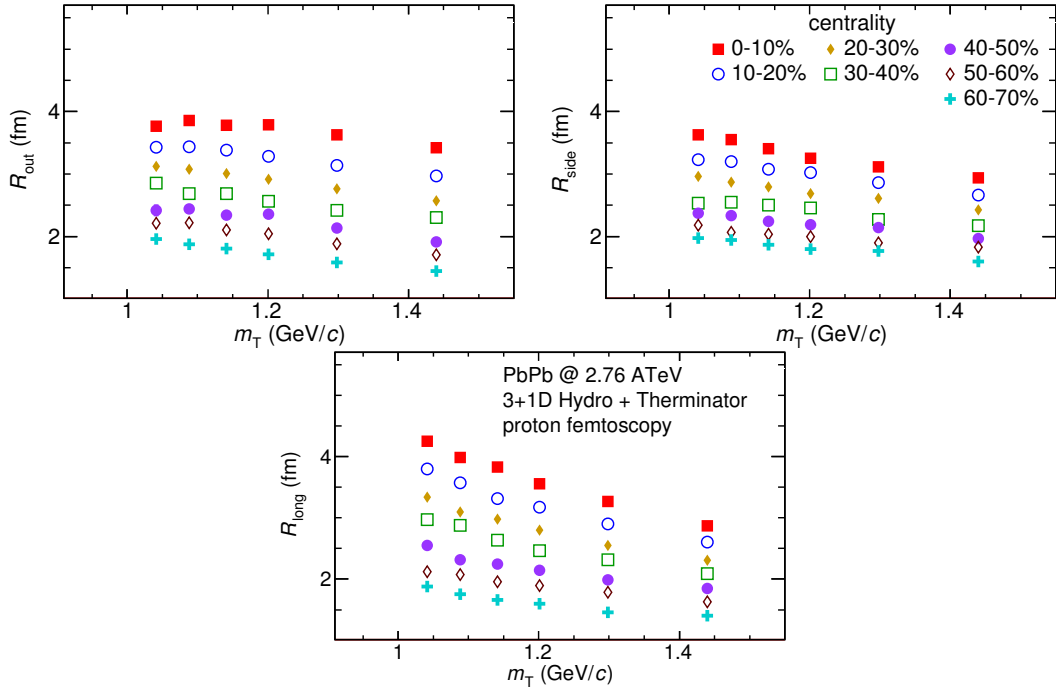


Figure 4.8: Femtoscopic radii extracted from two-proton correlation functions for different centrality bins as a function of m_T . [30].

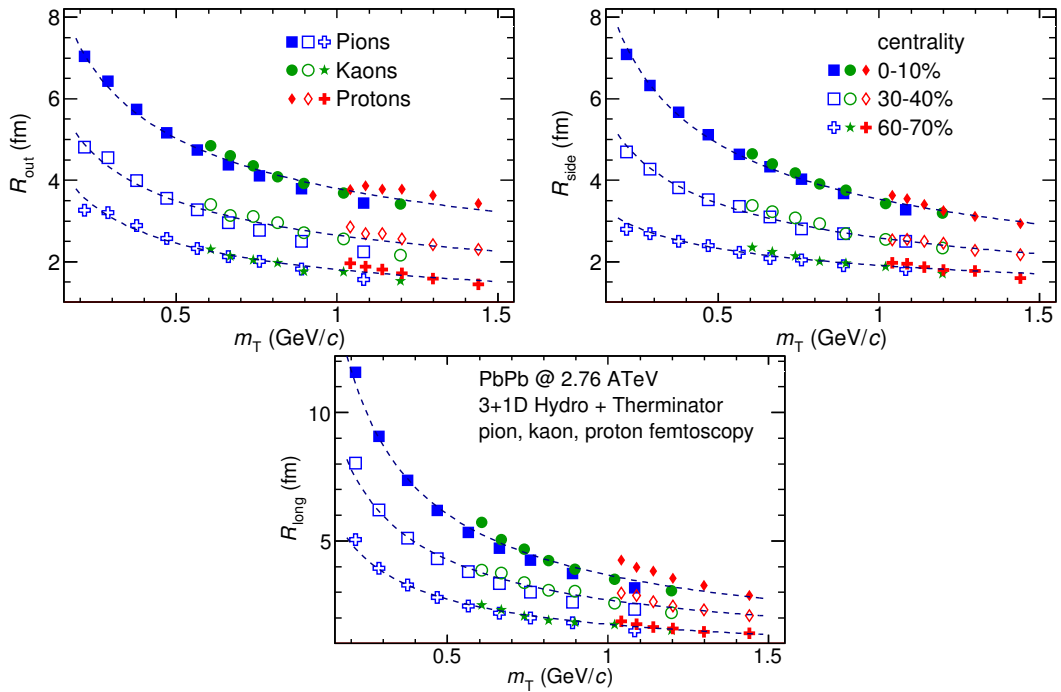


Figure 4.9: The results from the calculations for the pions, kaons and protons in for the three centralities presented on the common plot. One can notice that radii for particular centralities and different particle types follow the common power-law scaling. [30].

1020 **4.2.2 Scaling of one-dimensional radii**

1021 To the one-dimensional correlation function, the corresponding function in
 1022 the PRF given by the Eq. 3.18 was fitted. The results from those fits are presented
 1023 in the upper left plot in the Fig. 4.10. One immediately notices, that there is no
 1024 common scaling of R_{inv} for different kind of particles. In Fig. 4.9 the radii in the
 1025 outward direction for the pions, kaons and protons for the same m_T are similar.
 1026 However, when one performs a transition from the LCMS to the PRF, the R_{out}
 1027 radius grows:

$$R_{out}^* = \gamma_T R_{out}, \quad (4.2)$$

1028 where $\gamma_T = m_T/m$. For the lighter particles, the γ_T is much larger, hence the
 1029 bigger growth of the R_{out} and the overall radius. This is visible in the Fig. 4.10
 1030 (top left), where the radii in the PRF for the lighter particles are bigger than for
 1031 the heavier ones in case of the same m_T range.

1032 In the Fig. 4.9 there is visible scaling in the outward, sideward and longitudi-
 1033 nal direction. Hence one can expect an appearance of such scaling in a direction-
 1034 averaged radius calculated in the LCMS. This radius is presented in the Fig. 4.10
 1035 (bottom) and indeed the R_{LCMS} exhibits power-law scaling with m_T .

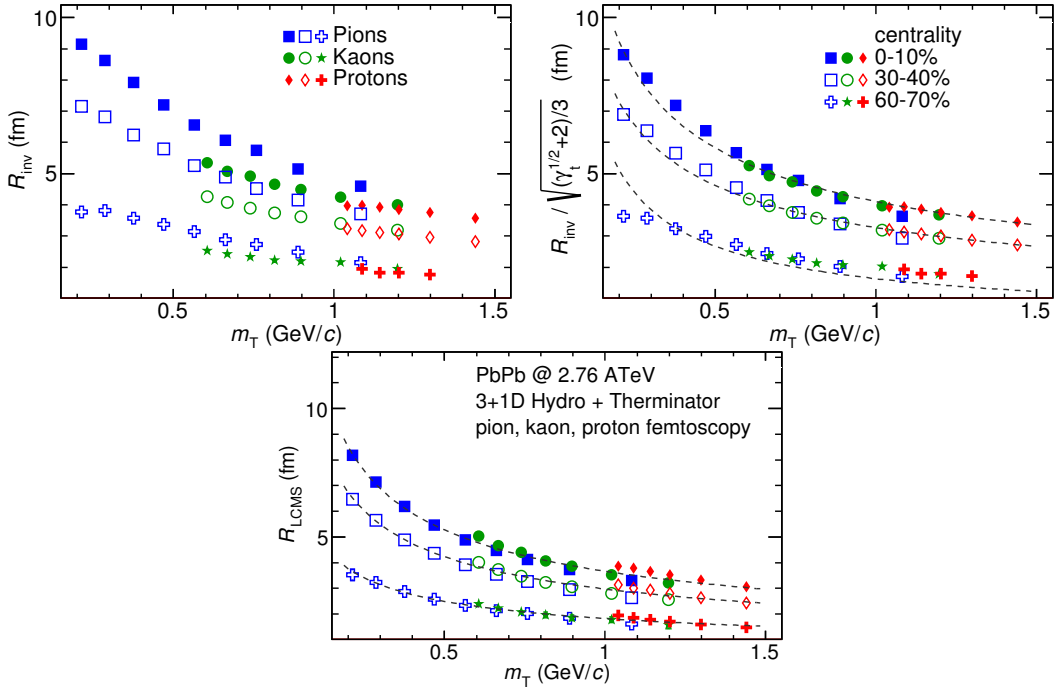


Figure 4.10: Top left: one-dimensional radius for pions, kaons and protons calcu-
 lated in the PRF. Top right: the R_{inv} scaled by the proposed factor. Bottom: av-
 eraged one-dimensional radius in the LCMS for pions, kaons and protons. Only
 three centrality bins are shown for the better readability [30].

1036 One can try to account the effect of an increase of the radii in the outward direction
 1037 by using the appropriate scaling factor. In Fig. 4.10 (top right), femtoscopic
 1038 radii in the LCMS are divided by the proposed scaling factor:

$$f = \sqrt{(\sqrt{\gamma_T} + 2)/3} . \quad (4.3)$$

1039 The radii for pions, kaons and protons in the PRF after the division by f are
 1040 following the power-law with the accuracy of 10%.

1041 4.3 Discussion of the results

1042 The femtoscopic radii obtained from the three-dimensional correlation func-
 1043 tion fitting exhibit the m_T dependence described by the power law (Eq. 4.1). This
 1044 scaling is preserved quite well with accuracy <10%. Observation of such scaling
 1045 in a femtoscopic radii is a strong signal of the appearance of a collective beha-
 1046 viour of a particle-emitting source created in the collision. The data used in the
 1047 analysis was coming from the hydrodynamic model, hence one can indeed ex-
 1048 pect the appearance of this scaling. However, the results for pion femtoscopy
 1049 from the ALICE at LHC are consistent with the data from analysis performed in
 1050 this thesis (Fig. 4.6). This is a confirmation of an applicability of hydrodynamic
 1051 models in a description of an evolution of a quark-gluon plasma.

1052 The β parameter calculated in the fitting of the power-law to the femtoscopic
 1053 radii is of the order of 0.5 in case of the radii in the transverse plane. This value is
 1054 consistent with the hydrodynamic predictions. In case of longitudinal radii, the
 1055 exponent is bigger (greater than 0.7), which is an indication of a strong transversal
 1056 expansion in the system [29].

1057 A scaling described above is visible in the LCMS, however due to limited
 1058 statistics, analysis in this reference frame is not always possible. In such case
 1059 one performs calculations in the PRF. The m_T scaling in the PRF is not observed
 1060 - this has a trivial kinematic origin. A transition from the PRF to LCMS causes
 1061 growth of the radius in the outward direction and the common power-law scal-
 1062 ing for different particles breaks due to differences in the $\gamma_T(m_T)$ for different
 1063 particle types. However one can try to deal with the radius growth and restore
 1064 the scaling by dividing the radii R_{inv} by an approximate factor $\sqrt{(\sqrt{\gamma_T} + 2)/3}$.
 1065 The scaled R_{inv} are following the power-law and could be used as a verification
 1066 of hydrodynamic behaviour in the investigated particle source.

1067 The hadronic evolution and freeze-out in the THERMINATOR is followed by
 1068 the resonance propagation and decay phase. A good accuracy of a scaling with
 1069 the power-law indicated that the inclusion of the resonances does not break the
 1070 m_T scaling. However, recent calculations, which include also hadron rescatter-
 1071 ing phase, indicate that the scaling between pions and kaons is broken at the
 1072 LHC [32]. Thus, the results of this work suggest that the scaling breaks at the
 1073 hadron rescattering phase [30].

Conclusions

This thesis presents the results of the two-particle femtoscopy of different particle kinds produced in Pb-Pb collisions at the centre of mass energy $\sqrt{s_{NN}} = 2.76$ TeV. The analysed data was generated by the THERMINATOR model using hypersurfaces from (3+1)-dimensional hydrodynamic calculations.

The momentum correlations were studied for three different types of particle pairs: pions, kaons and protons. The data was analyzed for eight different sets of initial conditions corresponding the following centrality ranges: 0-5%, 0-10%, 10-20%, 20-30%, 30-40%, 40-50%, 50-60% and 60-70%. The correlation functions were calculated for nine k_T bins from 0.1 GeV/c to 1.2 GeV/c. The calculations were performed using spherical harmonics decomposition of a three-dimensional correlation function. Using this approach, one can obtain full three-dimensional information about the source size using only the three coefficients: $\Re C_0^0$, $\Re C_2^0$ and $\Re C_2^2$. To perform further quantitative analysis, the femtoscopic radii were extracted through fitting.

The calculated correlation functions show expected increase of a correlation at low relative momenta in case of identical bosons (pions and kaons) and the decrease for the identical fermions (protons) respectively. This effect is especially visible in the first spherical harmonic coefficient $\Re C_0^0$. The other two components $\Re C_2^0$ and $\Re C_2^2$ are non-vanishing and are providing information about the ratios of radii in the outward, sideward and longitudinal directions.

An increase of width of a correlation function with the peripherality of a collision and the k_T is observed for pions, kaons and protons. This increase of femtoscopic radii (proportional to the inverse of width) with k_T is related with the m_T scaling predicted by the hydrodynamic calculations.

Hydrodynamic equations are predicting appearance of the common scaling of femtoscopic radii for different kinds of particles with $m_T^{-0.5}$ in the LCMS. In the results of this work, a common scaling for different particle types is observed in LCMS in the outward, sideward and longitudinal direction. The direction-averaged radius R_{LCMS} also shows this power-law behaviour. The fitting of a power law $\alpha m_T^{-\beta}$ to the femtoscopic radii yielded the information, that the β exponent for the outward and sideward direction is of the order of 0.5, which is consistent with the hydrodynamic predictions. For the longitudinal direction, the β is bigger (>0.7) than in the other directions which is an indication of a strong transverse flow. Femtoscopic radii in LCMS are following the power-law scaling

1109 with the accuracy $<5\%$ for pions and kaons, and $<10\%$ in case of protons.

1110 In case of the one-dimensional radii R_{inv} calculated in the PRF, no common
1111 scaling is observed. This is a consequence of a transition from the LCMS to the
1112 PRF, which causes the growth of radius in the outward direction and breaks the
1113 scaling for different particles. However, one can try to correct the influence of
1114 the R_{out} growth with an approximate factor $\sqrt{(\sqrt{\gamma_T} + 2)/3}$. After the division
1115 of the R_{inv} by the proposed factor, the scaling is restored with an accuracy $<10\%$.
1116 In this way, the experimentally simpler measure of the one-dimensional radii can
1117 be used as a probe for the hydrodynamic collectivity.

1118 The THERMINATOR model includes hydrodynamic expansion, statistical had-
1119 ronization, resonance propagation and decay afterwards. The m_T scaling is pre-
1120 dicted from the pure hydrodynamic calculations. However, this study shows,
1121 that influence of the resonances on this scaling is less than 10%.

1122 **Appendix A**

1123 **Scripts for correlation function
1124 calculations**

1125 **A.1 Events generation**

1126 In order to perform analysis with sufficient statistics, a big number of events
1127 was required. To handle this task of generation large amount of data, a computer
1128 cluster at Faculty of Physics at Warsaw University of Technology was used. This
1129 cluster consists of 20 nodes with the following hardware configuration: Intel®
1130 Core™ 2 Quad CPU Q6600 @ 2.40GHz, 8GB RAM with Scientific Linux 5.8.
1131 The communication between nodes is realized by the TORQUE Resource
1132 Manager [33]. To control process of launching multiple event generators and
1133 collecting the data, the following scripts were written using Bash scripting
1134 language:

1135 **skynet.sh** This is a script in a form of a batch job for TORQUE. It simply
1136 launches multiple THERMINATOR processes in the same working directory
1137 with the separate output directory for each job. This solution has two
1138 advantages: saves space and computation time. A single freeze-out
1139 hypersurface file has size about 230 MB and when running 20 instances
1140 of generator this approach allows to avoid time- and space-consuming
1141 copying of the whole THERMINATOR directory before running the
1142 application. The second advantage is sharing of files containing
1143 information about particles' multiplicities and maximum integrands
1144 between generator processes (more detailed description is in Section 2.3).
1145 One can simply execute this batch job using the following command (an
1146 example usage):

1147 `qsub -q long -t 0-19 skynet.sh -v dir=th_5.7,events=6000`
1148 It adds 20 event generators (with task ids from 0 to 19) to the queue, sets
1149 the THERMINATOR directory as `th_5.7` and sets a number of simulated
1150 events to 6000 for each process. One has to execute this command in the
1151 directory one level higher than `th_5.7` directory.

1152 **merge_events.sh** After the generation process, one has to merge calculated
 1153 events into one directory. This task requires renaming of a large number of
 1154 THERMINATOR event files. Each event generator job produces files named
 1155 with a certain pattern, starting from event000.root with increasing number.
 1156 In order to move the event files and preserve continuity in the numbering,
 1157 a simple script was written. An example of usage:

```
1158 find /data/source -iname "event*.root" -type f \
  1159 | merge_events.sh
```

1160 This command will find all the event files in the directory /data/source,
 1161 move and rename those files accordingly to the numeration of events in
 1162 the current working directory.

1163 Sources of these two scripts are available on-line at <https://github.com/carbolymer/msc/tree/master/alix>.

1165 A.2 Calculations of experimental-like correlation 1166 functions

1167 Correlation functions used in this analysis were calculated using **tpi**
 1168 software written by Adam Kisiel and designed for reading event files from
 1169 THERMINATOR. It uses ROOT library for calculations and storage of the data.
 1170 The application provides functionality of calculation of one-dimensional
 1171 correlation function in PRF, three-dimensional one in LCMS and its spherical
 1172 harmonics decomposition (see Section 3.2.5). The exact numerical procedure of
 1173 computation of a correlation function is presented in Section 3.3. **tpi** allows to
 1174 perform calculations with the following options:

- 1175 • Pair type - there are pion-pion, kaon-kaon, proton-proton and many more
 1176 pairs available (including ones consisting of non-identical particles)
- 1177 • Multiple k_T subranges from 0.21 to 1.2 GeV/c
- 1178 • Possibility to include Coulomb interaction
- 1179 • Number of events to mix
- 1180 • Maximum freeze-out time
- 1181 • Choice of method of background calculation in correlation function (mixing
 1182 events or using particles from the same event)

1183 This program generates results stored in the *.root files in a form of histograms.
 1184 Output file contains numerators, denominators and correlation functions from
 1185 one-dimensional and three-dimensional analysis. Moreover, the spherical har-
 1186 monics series coefficients up to $l = 3$ with signal and background histograms are
 1187 stored.

1188 **Appendix B**

1189 **Fitting utilities**

1190 Procedure of fitting analytical formulas to experimental-like correlation func-
1191 tions was performed using custom software written in C++ and Bash. This ap-
1192 plication utilizes MINUIT [34] package built in the ROOT library.

1193 **B.1 Minuit package**

1194 The MINUIT is a physics analysis tool for function minimization written in
1195 Fortran programming language. This tool was designed for statistical analysis
1196 and it is working on χ^2 or log-likelihood functions to compute the best-fit para-
1197 meter values and uncertainties, including correlations between parameters. It is
1198 implemented in ROOT environment as TMinuit class, which provides interface
1199 to the minimization tool. The analysis performed in this work uses MINUIT with
1200 the Migrad minimization method. The Migrad minimizer is the best one embed-
1201 ded in Minuit. It's a variable-metric method with inexact line search, a stable
1202 metric updating scheme, and checks for positive-definiteness [34].

1203 **B.2 Fitting software**

1204 Fitting utility provides tools for extraction of femtoscopic radii from correla-
1205 tion functions for identical particles. It provides also a macro for generating plots
1206 with these radii as a function of transverse mass and fitting power-law $\alpha m_T^{-\beta}$ to
1207 the results.

1208 **B.2.1 Input parameters**

1209 The application reads the output files from the tpi program and extracts
1210 from them one-dimensional and three-dimensional correlation functions. The
1211 latter ones are in a form of spherical harmonics series coefficients.

1212 One has also a possibility to set fit parameters for certain centrality bins, pair
1213 types and k_T ranges. Configuration files (*.conf) are located inside the applica-

tion's folder in the `data/` directory. Files with the names beginning with `fitsh` contain parameters for three-dimensional fits, while `fit1d` prefix indicates settings for one-dimensional ones. File `fitsh.kk.conf` contains initial parameters for all fits for pairs of kaons. Similarly, one can set fit parameters for pions (`pipi`) and protons (`pp`) using corresponding letters in place of `kk` in the name of the file.

Here is an example parameter file for one-dimensional fit (`fit1d`):

1.0	L	normalization
1.0	L	λ
4.0	L	R_{inv}
0.0	F	not used

The `F` letter after the parameter indicates that it is a fixed value (will not change during fitting process), whereas the `L` parameter tells that this value will be modified.

An example parameter file for three-dimensional fit (`fitsh`):

4.5	L	1.2	5.5	R_{out} in fm
4.5	L	1.2	5.5	R_{side} in fm
4.5	L	1.2	6.5	R_{long} in fm
0.70	L	0.2	2.2	λ
1.14	F	1.14	1.14	C_2^0 coefficient
1.25	F	1.25	1.25	C_2^2 coefficient
1.0	L	0.8	1.2	overall normalization
0.0	F	0.0	0.0	C_2^0 normalization
0.0	F	0.0	0.0	C_2^2 normalization
0.25	F	0.25	0.25	q_{beg}
0.25	F	0.25	0.25	q_{slope}
0.0	F	0.0	0.0	not used
0.0	F	0.0	0.0	not used
0.0	F	0.0	0.0	not used
0.0	F	0.0	0.0	not used
0.0	F	0.0	0.0	not used
0.0	F	0.0	0.0	not used
0.0	F	0.0	0.0	not used
0.0	F	0.0	0.0	not used
IdLCY1m				correlation function numerator name
0.0075				beginning of the fitting range (q in GeV/c)
0.2				end of the fitting range (q in GeV/c)

0	not used

1224 This file contains extra columns indicating allowed range for value of a fit
 1225 parameter. The first number (the 3rd column) is the minimum and the second
 1226 one (4th column) is the maximum of this range.

1227 B.2.2 Output format

1228 The application during calculations creates inside `data/` directory, subdirectories
 1229 for each centrality. For each pair type and each of the following variables
 1230 R_{inv} , R_{out} , R_{side} , R_{long} , λ and R_{LCMS} , the output files `*.out` with four columns are
 1231 created. First column is the beginning of the k_T range, second one is the ending
 1232 of the range, third column contains result of the fit and the last one stores un-
 1233 certainty of this value. In addition, plots (in the png format) of the correlation
 1234 functions for each pair type and k_T bin are generated inside subdirectories.

1235 Files `filelist.{pair type}.in` contain list of input `*.root` files with processed corre-
 1236 lation functions.

1237 B.2.3 Compilation

1238 This utility requires ROOT framework and `libboost-regex-dev` library.
 1239 Compilation can be performed using `make` command inside application's dir-
 1240 ectory.

1241 B.2.4 Usage

1242 Fitting process

1243 In order to perform the fitting process, one should execute the following com-
 1244 mand:

1245 `./run.sh /path/to/the/tpi/output centrality`

1246 The `/path/to/the/tpi/output` parameter is a location of tpi output files
 1247 and `centrality` is a name of a directory in which the results of fits will be
 1248 stored.

1249 Plotting

1250 In order to plot femtoscopic radii and perform fitting of power law, one has
 1251 to use the following command:

1252 `make plots`

1253 Plots will be generated in the `output` directory.

1254 The source of fitting software is available on-line at <https://github.com/carbolymmer/msc/tree/master/fitting>.

1256 **Appendix C**

1257 **Plotting scripts**

1258 **C.1 Correlation functions plots**

1259 Plots containing correlation functions were generated using two ROOT macros
1260 written in C++.

1261 The first one, **cf1DAllCentralities.C** generates two plots with one-dimen-
1262 sional correlation functions. First plot presents k_T dependence of a correlation
1263 function and is saved in the *cfvskt.eps* file, and the second one shows influence
1264 of centrality on a correlation function (saved in the *cfvsctr.eps* file). In order to
1265 generate plots one has to set in the line 9, the path to the folder which contains
1266 sub-directories with files containing correlation functions. One can produce eps
1267 files, using the following command:

1268 `root -l -b -q cf1DAllCentralities.C`

1269 *cfvskt.eps* and *cfvsctr.eps* files will be generated in the current working directory.

1270 The second macro, **cf3DAllCentralities.C** produces plots with spherical har-
1271 monics coefficients for pions (*cf3dpi.eps*), kaons (*cf3dk.eps*) and protons (*cf3dp.eps*).
1272 This script has similar structure to the previous one. In order one has to set the
1273 proper path in the line 18 also. To execute this macro, one can use the following
1274 command:

1275 `root -l -b -q cf3DAllCentralities.C`

1276 As a result, the three files with the output plots will be generated in the current
1277 working directory.

1278 The sources of these plotting macros are available on-line on <https://github.com/carbolymer/msc/tree/develop/fitting/macros>.

1280 **C.2 Plots with femtoscopy radii**

1281 Femtoscopy radii plots can be generated using fitting tool described in Ap-
1282 pendix B. To do so, one has to invoke the following command:

1283 `make plots`

1284 This command invokes ROOT macro *src/plotter.C* which generates all plots for the

every centrality automatically. This macro reads the femtoscopic radii for each pair type, k_T centrality bin and calculates the transverse mass for each particle kind. Thereafter, to all of the femtoscopic radii as a function of transverse mass, the following formula is fitted: $R_x = \alpha m_T^{-\beta}$. It should be noted, that the fitting is performed to the radii of pions, kaons and protons together. As a result of the fit, for the each centrality, plot with femtoscopic radii in the outward, sideward, and longitudinal direction as well as overall radii is generated. Moreover, the comparison between different centralities in PRF divided by the scaling factor (see Section 3.4) and the R_{LCMS} is also plotted.

¹²⁹⁴ Bibliography

- ¹²⁹⁵ [1] Standard Model of Elementary Paticles - Wikipedia, the free encyclopedia
¹²⁹⁶ http://en.wikipedia.org/wiki/Standard_Model.
- ¹²⁹⁷ [2] R. Aaij et al. (LHCb Collaboration). Observation of the resonant character of
¹²⁹⁸ the $z(4430)^-$ state. *Phys. Rev. Lett.*, 112:222002, Jun 2014.
- ¹²⁹⁹ [3] Donald H. Perkins. *Introduction to High Energy Physics*. Cambridge University Press,
¹³⁰⁰ fourth edition, 2000. Cambridge Books Online.
- ¹³⁰¹ [4] G. Odyniec. *Phase Diagram of Quantum Chromo-Dynamics* - course at Faculty
¹³⁰² of Physics, Warsaw University of Technology, Jun 2012.
- ¹³⁰³ [5] J. Beringer et al. (Particle Data Group). The Review of Particle Physics. *Phys.*
¹³⁰⁴ *Rev.*, D86:010001, 2012.
- ¹³⁰⁵ [6] Z. Fodor and S.D. Katz. The Phase diagram of quantum chromodynamics.
¹³⁰⁶ 2009.
- ¹³⁰⁷ [7] F. Karsch. Lattice results on QCD thermodynamics. *Nuclear Physics A*, 698(1-
¹³⁰⁸ 4):199 – 208, 2002.
- ¹³⁰⁹ [8] Adam Kisiel. *Studies of non-identical meson-meson correlations at low relative ve-*
¹³¹⁰ *locities in relativistic heavy-ion collisions registered in the STAR experiment*. PhD
¹³¹¹ thesis, Warsaw University of Technology, Aug 2004.
- ¹³¹² [9] J. Bartke. *Relativistic Heavy Ion Physics*. World Scientific Pub., 2009.
- ¹³¹³ [10] W. Florkowski. *Phenomenology of Ultra-Relativistic Heavy-Ion Collisions*.
¹³¹⁴ World Scientific, 2010.
- ¹³¹⁵ [11] Science Grid This Week, October 25, 2006 - Probing the Perfect Liquid with
¹³¹⁶ the STAR Grid [http://www.interactions.org/sgtw/2006/1025/](http://www.interactions.org/sgtw/2006/1025/star_grid_more.html)
¹³¹⁷ [star_grid_more.html](http://www.interactions.org/sgtw/2006/1025/star_grid_more.html).
- ¹³¹⁸ [12] K. Grebieszkow. Fizyka zderzeń ciężkich jonów, <http://www.if.pw.edu.pl/~kperl/HIP/hip.html>.
- ¹³²⁰ [13] Ulrich W. Heinz. From SPS to RHIC: Maurice and the CERN heavy-ion
¹³²¹ programme. *Phys.Scripta*, 78:028005, 2008.

- 1322 [14] J. Adams et al. Identified particle distributions in pp and Au+Au collisions
1323 at $s_{\text{NN}}^{**}(1/2) = 200 \text{ GeV}$. *Phys.Rev.Lett.*, 92:112301, 2004.
- 1324 [15] G. David, R. Rapp, and Z. Xu. Electromagnetic Probes at RHIC-II. *Phys.Rept.*,
1325 462:176–217, 2008.
- 1326 [16] A. Marin et al. Dilepton measurements with CERES. *PoS*, CPOD07:034,
1327 2007.
- 1328 [17] J. Adams et al. Experimental and theoretical challenges in the search for the
1329 quark gluon plasma: The STAR Collaboration’s critical assessment of the
1330 evidence from RHIC collisions. *Nucl.Phys.*, A757:102–183, 2005.
- 1331 [18] Adam Kisiel, Tomasz Taluc, Wojciech Broniowski, and Wojciech
1332 Florkowski. THERMINATOR: THERMal heavy-IoN generATOR. *Comput.Phys.Commun.*, 174:669–687, 2006.
- 1334 [19] Mikolaj Chojnacki, Adam Kisiel, Wojciech Florkowski, and Wojciech Bro-
1335 niowski. THERMINATOR 2: THERMal heavy IoN generATOR 2. *Comput.
1336 Phys.Commun.*, 183:746–773, 2012.
- 1337 [20] ROOT - A Data Analysis Framework <http://root.cern.ch/drupal/>.
- 1338 [21] I. et al (BRAHMS Collaboration) Bearden. Charged meson rapidity distri-
1339 butions in central Au + Au collisions at $\sqrt{s_{\text{NN}}} = 200 \text{ GeV}$. *Phys. Rev. Lett.*,
1340 94:162301, Apr 2005.
- 1341 [22] W. Israel and J.M. Stewart. Transient relativistic thermodynamics and kin-
1342 etic theory. *Annals of Physics*, 118(2):341 – 372, 1979.
- 1343 [23] Piotr Bożek. Flow and interferometry in (3 + 1)-dimensional viscous hydro-
1344 dynamics. *Phys. Rev. C*, 85:034901, Mar 2012.
- 1345 [24] K. Kovtun, P. D. T. Son, and A. O. Starinets. Viscosity in strongly interacting
1346 quantum field theories from black hole physics. *Phys. Rev. Lett.*, 94:111601,
1347 Mar 2005.
- 1348 [25] Fred Cooper and Graham Frye. Single-particle distribution in the hydro-
1349 dynamic and statistical thermodynamic models of multiparticle production.
1350 *Phys. Rev. D*, 10:186–189, Jul 1974.
- 1351 [26] Adam Kisiel. Nonidentical-particle femtoscopy at $\sqrt{s_{\text{NN}}} = 200 \text{ GeV}$ in hy-
1352 drodynamics with statistical hadronization. *Phys. Rev. C*, 81:064906, Jun
1353 2010.
- 1354 [27] Adam Kisiel and David A. Brown. Efficient and robust calculation of femto-
1355 scopic correlation functions in spherical harmonics directly from the raw
1356 pairs measured in heavy-ion collisions. *Phys.Rev.*, C80:064911, 2009.

- 1357 [28] S. Pratt. Pion Interferometry for Exploding Sources. *Phys.Rev.Lett.*, 53:1219–
1358 1221, 1984.
- 1359 [29] S.V. Akkelin and Yu.M. Sinyukov. The HBT-interferometry of expanding
1360 inhomogeneous sources. *Z.Phys.*, C72:501–507, 1996.
- 1361 [30] A. Kisiel, M. Galazyn, and P. Bozek. Pion, kaon, and proton femtoscopy in
1362 Pb–Pb collisions at $\sqrt{s_{NN}}=2.76$ TeV modeled in 3+1D hydrodynamics. 2014.
- 1363 [31] K. Aamodt et al. Two-pion Bose-Einstein correlations in central Pb-Pb colli-
1364 sions at $\sqrt{s_{NN}} = 2.76$ TeV. *Phys.Lett.*, B696:328–337, 2011.
- 1365 [32] V.M. Shapoval, P. Braun-Munzinger, Iu.A. Karpenko, and Yu.M. Sinyukov.
1366 Femtoscopy correlations of kaons in $Pb + Pb$ collisions at LHC within hy-
1367 drokinetic model. 2014.
- 1368 [33] TORQUE Resource Manager - An open source resource manager provid-
1369 ing control over batch jobs and distributed compute nodes <http://www.adaptivecomputing.com/products/open-source/torque/>.
- 1370 [34] MINUIT - Function Minimization and Error Analysis <http://wwwasdoc.web.cern.ch/wwwasdoc/minuit/minmain.html>.

List of Figures

1374	1.1	The Standard Model of elementary particles [1].	3
1375	1.2	A string breaking and a creation of a new quark-anti-quark pair [4].	5
1376	1.3	The coupling parameter α_s dependence on four-momentum transfer Q^2 [5].	6
1377	1.4	The QCD potential for a quark-antiquark pair as a function of distance for different temperatures. A value of a potential decreases with the temperature [4].	7
1378	1.5	A number of degrees of freedom as a function of a temperature [7].	7
1379	1.6	Phase diagram coming from the Lattice QCD calculations [8].	8
1380	1.7	Left: stages of a heavy ion collision simulated in the UrQMD model. Right: schematic view of a heavy ion collision evolution [8].	9
1381	1.8	Overlapping region which is created in heavy ion collisions has an almond shape. Visible x-z plane is a <i>reaction plane</i> . The x-y plane is a <i>transverse plane</i> . The z is a direction of the beam [11].	11
1382	1.9	Cross-section of a heavy ion collision in a transverse plane. The b parameter is an <i>impact parameter</i> - a distance between centers of nuclei during a collision. An impact parameter is related with the centrality of a collision and a volume of the quark-gluon plasma [12].	12
1383	1.10	<i>Lower:</i> The elliptic flow v_2 follows the hydrodynamical predictions for an ideal fluid perfectly. Note that > 99% of all final hadrons have $p_T < 1.5 \text{ GeV}/c$. <i>Upper left:</i> The v_2 plotted versus transverse kinetic energy $KE_T = m_T - m_0 = \sqrt{p_T^2 + m_0^2} - m_0$. The v_2 follows different universal curves for mesons and baryons. <i>Upper right:</i> When scaled by the number of valence quarks, the v_2 follows the same universal curve for all hadrons and for all values of scaled transverse kinetic energy [13].	13
1384	1.11	Invariant yield of particles versus transverse mass $m_T = \sqrt{p_T^2 + m_0^2}$ for π^\pm , K^\pm , p and \bar{p} at mid-rapidity for p+p collisions (bottom) and Au+Au events from 70-80% (second bottom) to 0-5% (top) centrality [14].	14

1404	1.12 Thermal photons spectra for the central Au+Au collisions at $\sqrt{s_{NN}} = 200$ GeV computed within different hydrodynamical models compared with the pQCD calculations (solid line) and experimental data from PHENIX (black dots) [15].	15
1405		
1406		
1407		
1408	1.13 Left: Invariant mass spectrum of e^+e^- pairs in Pb+Au collisions at 158A GeV compared to the sum coming from the hadron decays predictions. Right: The expectations coming from model calculations assuming a dropping of the ρ mass (blue) or a spread of the ρ width in the medium (red) [16].	16
1409		
1410		
1411		
1412		
1413	1.14 Azimuthal angle difference $\Delta\phi$ distributions for different colliding systems at $\sqrt{s_{NN}} = 200$ GeV. Transverse momentum cut: $p_T > 2$ GeV. For the Au+Au collisions the away-side jet is missing [17]. . .	17
1414		
1415		
1416	2.1 The cascade decay in the single freeze-out model. An unstable resonance x_N is formed at the freeze-out hypersurface and travels for the time τ_N depending on its lifetime and decays. If the products are also resonances (x_{N-1}, x_2) they decay further until the stable particles are formed (x_1) [18].	24
1417		
1418		
1419		
1420		
1421	3.1 Bertsch-Pratt direction naming convention used in heavy ion collision.	26
1422		
1423	3.2 The pair wave function is a superposition of all possible states. In case of particle interferometry it includes two cases: particles with momenta p_1, p_2 registered by detectors A, B and p_1, p_2 registered by B, A respectively.	27
1424		
1425		
1426		
1427	3.3 An averaged three-dimensional Gaussian source function with different widths was averaged into one-dimensional function. To illustrate deformations, one-dimensional Gaussian distribution was fitted.	30
1428		
1429		
1430		
1431	3.4 Correlation function width dependence on total pair momentum. Pion pairs with a large total momentum have a wider correlation (smaller apparent source) [28].	34
1432		
1433		
1434	4.1 Spherical harmonics coefficients of the two-pion correlation function. From the top left: $\Re C_0^0$, $\Re C_2^0$ and $\Re C_2^2$. Only few centrality bins are presented for increased readability.	37
1435		
1436		
1437	4.2 Spherical harmonics coefficients of the two-kaon correlation function. From the top left: $\Re C_0^0$, $\Re C_2^0$ and $\Re C_2^2$. Only few centrality bins are presented for increased readability. The $\Re C_2^2$ is noisy, but one can still notice that it differs from zero and is becoming negative.	38
1438		
1439		
1440		

1441	4.3 Spherical harmonics coefficients of the two-proton correlation function. From the top left: $\Re C_0^0$, $\Re C_2^0$ and $\Re C_2^2$. Only few centrality bins are presented for increased readability. The $\Re C_2^0$ and $\Re C_2^2$ are noisy, but one can still notice, that they differ from zero and are becoming positive.	39
1442		
1443		
1444		
1445		
1446	4.4 One-dimensional correlation function for pions (top left), kaons (top right) and protons (bottom) for different centralities.	40
1447		
1448		
1449		
1450		
1451		
1452		
1453	4.5 One-dimensional correlation functions for pions, kaons and protons, for the same centrality bin and different k_T ranges. The plot was zoomed in to the region which illustrates the k_T dependence in the best way. Only few of the calculated ranges are presented for better readability.	41
1454		
1455		
1456		
1457		
1458	4.6 Femtoscopic radii in LCMS coming from two-pion correlation functions for all centrality bins as a function of m_T . The dashed lines are power-law fits. The most central collisions (0-5%) are compared to the results from ALICE [31]. The two datasets are shifted to the right for visibility [30].	42
1459		
1460		
1461		
1462	4.7 Femtoscopic radii extracted from two-kaon correlation functions for different centrality bins as a function of m_T . [30].	43
1463		
1464		
1465	4.8 Femtoscopic radii extracted from two-proton correlation functions for different centrality bins as a function of m_T . [30].	44
1466		
1467	4.9 The results from the calculations for the pions, kaons and protons in for the three centralities presented on the common plot. One can notice that radii for particular centralities and different particle types follow the common power-law scaling. [30].	45
1468		
1469		
1470	4.10 Top left: one-dimensional radius for pions, kaons and protons calculated in the PRF. Top right: the R_{inv} scaled by the proposed factor. Bottom: averaged one-dimensional radius in the LCMS for pions, kaons and protons. Only three centrality bins are shown for the better readability [30].	46